The Influence of Development and Fan/Screen Interaction on Screen-Generated Total Pressure Distortion Profiles

Justin Mark Bailey

Thesis submitted to the Faculty of the
Virginia Polytechnic Institute and State University
in partial fulfillment of the requirements for the degree of

Master of Science
in
Mechanical Engineering

Walter F. O'Brien, Chair
Clinton L. Dancey
Alfred L. Wicks

December 5, 2013
Blacksburg, Virginia

Keywords: Total Pressure Distortion Development, Fan/Screen Interaction, Wire-mesh Screens

The Influence of Development and Fan/Screen Interaction on Screen-Generated Total Pressure Distortion Profiles

Justin M. Bailey

Abstract

The rising interest in fan performance in the presence of total pressure distortion, a topic of fundamental interest for integrated airframe/engine architectures, has led to increased research in ground based testing environments. Included in these studies is the generation of simulated total pressure distortion profiles using wire mesh screens. Although the inlet duct development of total pressure distortion patterns has been studied in a historical context when distortion effects on engine performance were first of interest, these were typically simplified experimental studies for low-speed flows. To aid in the understanding of total pressure distortion development approaching a transonic fan face, a series of experiments were conducted to detail the development of such a profile downstream of the screen plane in the absence and presence of fan effects.

Presented is an extensive experimental set to detail (1) the evolution of a screen-generated total pressure distortion profile as it develops in a constant diameter inlet duct and (2) the effect that a single stage transonic fan has on the distortion development. Included is a detailed analysis of the distortion profile characteristics for increasing development length, and the behavioral changes of the profile when fan blockage is present near the screen plane. Recommendations are made regarding the placement of total pressure distortion screens relative to the fan face, and insights are given into the expected profile evolution. This work is a contributing part of an ongoing systematic investigation of fan performance when subjected to screen-generated total pressure inlet distortion.

Acknowledgements

I wish first to thank NASA and the United Technologies Corporation under subcontract 11-S590-0020-19-C1 for the financial support of this research, without which these experiments would not have been possible. I would also like to thank Dr. William Copenhaver at the Air Force Research Laboratory for his technical assistance and expertise.

My sincere gratitude is offered to the members of my thesis committee: Dr. Walter O'Brien, Dr. Clinton Dancey, and Dr. Wing Ng of Virginia Tech. Your assistance and support are much appreciated. Thank you for your dedication to research, but most importantly for your investment in guiding the next generation of engineers.

To my current and former colleagues of the Virginia Tech Turbomachinery and Propulsion Research Laboratory: Tony Ferrar, Bill Schneck, Todd Pickering, Steven Steele, James Lucas, Kevin Hoopes, and Chris Collins. Working with you has been a pleasure and privilege and I thank each of you for your contributions to this work. Thank you for the discussions, insights, and all the assistance you have provided. Working in the VT Turbolab has been a terrific experience and I am most grateful to have had the opportunity to work alongside you all.

To my Mother and Father, Polly and Mark Bailey: Thank you for your patience, guidance, and advice during my time here at Virginia Tech. During one of my internships when I was an undergraduate student, a fellow employee once told me, "If you're gonna put your name on it, *you* make sure it's right." While I try to adhere to this advice when claiming ownership of my work, such as this thesis, I find it more important to remember that my work is a reflection of our family and in particular yourselves, the individuals who raised me. I always try to put my best effort into everything I do so that you will be proud of the work our name is attached to.

To my sisters April, Meredith, and Hannah: While I do not always show it, I am most grateful to be your brother and I strive to be a person of integrity that you can be proud of. You give me a great deal of satisfaction when you relay stories about how impressed your friends are that 'My brother works for NASA', even if that is not technically accurate.

Table of Contents

Nomenclature

A/D	Analog to Digital
AIP	Aerodynamic Interface Plane
BDC	Bottom Dead Center
BLI	Boundary Layer Ingestion/Ingesting
LSB	Least Significant Bit
M	Mach number
PAV	Ring-average total pressure
PAVLOW	Average total pressure within deficit region
PFAV	AIP average total pressure
θ	Circumferential position [degrees]
θ^-	Circumferential distortion extent [degrees]
Re	Reynolds number
TDC	Top Dead Center
TPRA	Total Pressure Rake Array
u	Axial velocity [in/sec]
$\bar{x}$	Sample mean
y	Vertical distance from boundary layer wall [inches]
δ	Boundary layer thickness [inches]
μ	dynamic viscosity [lbs/ft^2]
σ	Sample standard deviation
τ	Shear stress [psi]

List of Figures

List of Tables

Chapter 1 - Introduction

In order to define fan performance subject to total pressure inlet distortion, fan outlet conditions have to be compared to their respective inlet conditions, which are a direct result of the evolution of a total pressure distortion profile as it traverses the inlet up to the fan face. In ground testing, it is also necessary to determine if the flow development upstream of the fan face is an accurate representation of real inlet conditions. Detailed performance measurements, including three dimensional velocity components, two-dimensional unsteady effects, and turbulence require the correct fan face flow profile, which evolves from what is measured at the Aerodynamic Interface Plane (AIP) and is dependent on the distance of the screen plane relative to the fan face.

The goal of this thesis research was to investigate the development of a total pressure distortion profile in a constant diameter varying length inlet duct from the screen plane to the fan face. Presented is (1) a detailed analysis into the flow development of a screen-produced total pressure distortion profile and (2) the effect of rotor presence on the development of this profile. Typically, a distortion screen is produced and tested, or calibrated, in a wind tunnel configuration that does not include fan effects that will be present in the engine ground test. An AIP is established, often one diameter upstream of the fan face, that specifies where this distortion profile is expected to occur. It is the screen designer's goal to generate a distortion at the AIP that simulates the desired profile. The screen is generally designed to incorporate a development length of one duct diameter. Therefore, in wind tunnel screen development, a total pressure rake is placed one diameter downstream of the screen to measure how the profile develops and to verify proper screen function. Once the distortion profile produces satisfactory results, the screen itself is typically placed one diameter upstream of the engine face, where it is assumed that the total pressure profile that was produced one diameter downstream in the wind tunnel configuration (measured by the total pressure rake) is equivalent to the profile reaching the fan face during engine testing.

A potential flaw in this process is the assumption that the screen performs equally in both testing configurations, that is, with and without the downstream fan presence. The fan introduces a downstream potential effect on the flow that produces a static pressure gradient in the tunnel, reaching a maximum at the fan face. This alters the behavior of any oncoming flow, producing distortion profiles that differ from those that were designed and calibrated in wind tunnel testing.

This study examines the rotor influence on the behavior of the distortion profile. In accordance with this analysis, an in-depth study of distortion profile development in an engine inlet duct is presented, and recommendations are given regarding screen positioning relative to the rotor. With the knowledge of how the flow develops in the presence and absence of the rotor, better design decisions can be made when (1) testing and calibrating the distortion screen and (2) determining the optimal screen plane location during experimentation.

Literature Review

Development in the field of combined engine/airframe technology has demonstrated the numerous benefits of engine/inlet integration for future commercial transport vehicles, a design inspired from modern military aircraft, albeit for different reasons such as low observability and radar avoidance. One such architecture that shows promise in improved fuel consumption, emissions, and noise production is the blended wing-body airframe, shown in Figure 1-left. The design incorporates boundary layer ingesting embedded engines with serpentine inlets. The inlet geometry is shown in Figure 1-right [1-4].

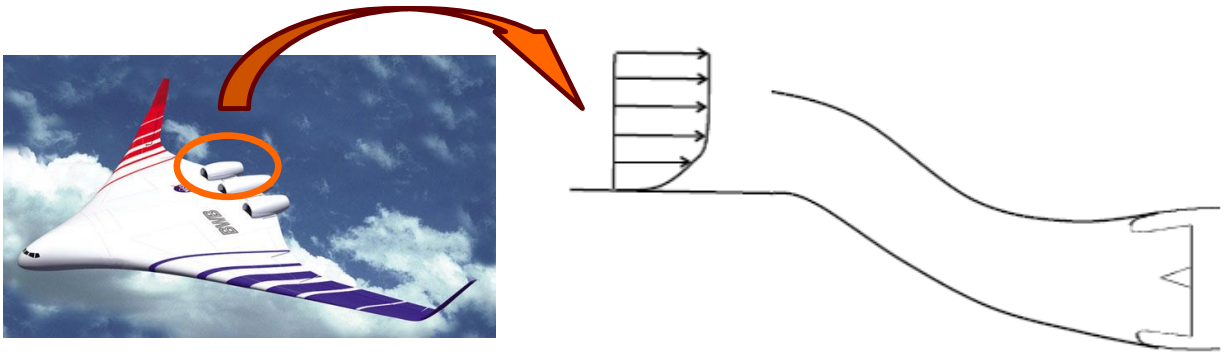

Figure 1. Blended wing body aircraft (left) and embedded engine system with serpentine ingesting inlet (right). [Courtesy: NASA]

A consequence of the boundary layer ingestion (BLI) and/or streamline curvature within serpentine inlets is the resulting generation of non-uniform, or distorted profiles. These profiles can take the form of total pressure, total temperature, or swirl (flow angularity) distortion. Such distortions can, if severe enough, lead to aerodynamic losses, decreased stability margin, and increased aeromechanical fatigue on the turbomachinery, in particular the fan and low pressure compressors. Total pressure distortions have received the most attention due to their frequent presence in curved intakes, and also when resulting from large angles of attack during take-off and strong crosswinds, or rapid flight maneuvers for military aircraft. Total pressure distortions are grouped in three categories; radial, circumferential, and a combination of the two (Figure 2).

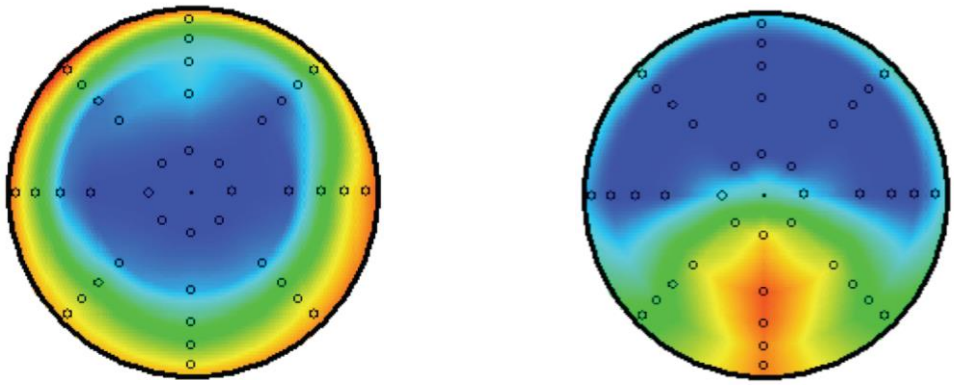

Figure 2. Examples of radial (left) and combined (right) total pressure distortion patterns [6].

Detailed, accurate knowledge of interactions between embedded engines and inlet/airframe-generated nonuniform flow profiles is essential for the successful design of robust integrated engine systems. Experimentation and research on the engine/inlet performance is either done using ground-test facilities or in-flight tests. Ground testing of engine-distortion interaction is typically performed using one of two methods. First, direct-connect methods involve testing the actual inlet/engine configuration in a realistic environment that must accurately simulate the effects of inlet spill, flow interactions with the airframe, and engine operation. This requires a large, full flight speed wind tunnel. In lieu of direct-connect experiments, a second method involves simulating the flowfield with distortion-producing devices. These devices are placed upstream of the engine and, if designed correctly, can effectively simulate the operating environment

of the engine/airframe system. This test method reduces the cost and increases control over the distortion pattern when compared to direct-connect experimentation.

Several architectures have been applied to generate flow distortions for ground testing engine performance. The most common approach involves the utilization of wire-mesh screens. Traditionally, wire-mesh screens installed on a supporting grid have been used to create steady total pressure distortions [6]. These screens utilize sections of constant-porosity wire meshes assembled to form radial, circumferential, or combined total pressure distortion profiles, as shown in Figure 3.

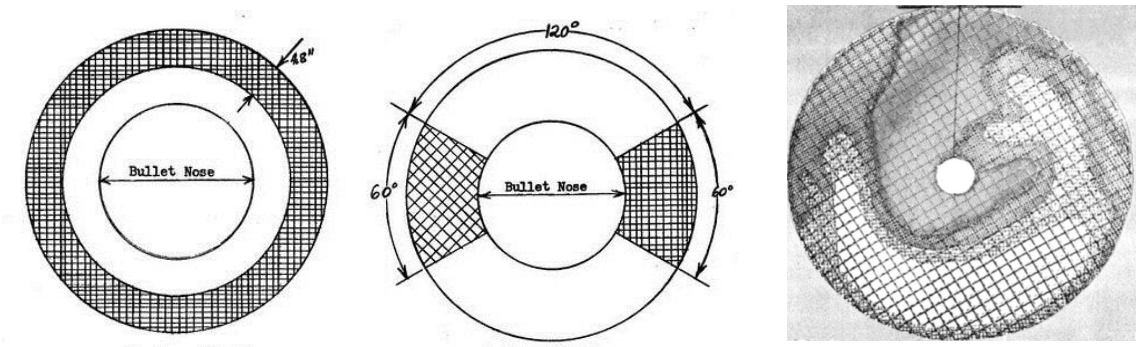

Figure 3. Radial (left), circumferential (center), and combined total pressure distortion screens (right). [5,10]

. The formation of specific profiles to mimic realistic environments is an understudied part of the engine/airframe interaction. Although research into distortion screen design began decades ago [5], recent interest in their flow profile generation and impact on testing procedures has once again produced an active area of research [7, 8]. One of the aspects of distortion profile testing that has not been considered in recent studies is the development of these profiles downstream of the screen plane, and how the fan presence alters this development. This interaction must be evaluated in further detail to fully understand the behavior of distortion profiles in the presence of turbomachinery. A majority of recent work has been allocated to analyzing the effect of distortion through a compressor stage [9-13], but very little research has investigated the upstream conditions of the distortion profile and how the distortion profile evolves near a fan or compressor.

Early work by Pearson and McKenzie [18] noted that when a total pressure distortion with a uniform static pressure was introduced far upstream of an axial flow compressor, a flow redistribution occurred upstream because of the presence of the compressor, and the static pressure profile changed as the flow approached the compressor face. A parallel compressor model was used to demonstrate that when the airflow into a compressor is distorted, the velocity at the inlet to the compressor will be virtually constant with consequent variations in the static pressure.

Callahan [25] developed a theoretical model for the flow redistribution upstream of an axial flow compressor operating with a total pressure distortion originating far upstream. ‘Long’ and ‘Short’ compressors were identified, where the former is indicative of constant static pressure at the compressor exit for all circumferential and radial locations, and the latter references compressor exit conditions that remain distorted. Flow redistribution occurred exclusively upstream for the ‘Long’ compressor case, as radial forces within the compressor have sufficient time to attenuate the distortion and result in a uniform exit static pressure. For the ‘Short’ compressor case, the radial velocity variation in the flow field was not completely eliminated by a single compressor stage, and was still present at the exit, contributing to cross-flow.

Plourde and Stenning [17] found in their upstream analysis that the flow redistribution was dependent upon the slope of the pressure rise-mass flow rate characteristic of the compressor. In low hub-tip ratio compressors the pressure rise characteristic can vary from root to tip along the blades. The inlet distortion may vary in the radial as well as the circumferential direction at its origin, with the conclusion that analyses considering this flowfield had to account for these three-dimensional effects.

Callahan and Stenning [19] described upstream flowfield behavior analytically and conducted a validation experiment of a low hub-tip ratio compressor operating with a circumferential total pressure distortion that originated two compressor tip radii upstream of the fan face. The experimental facility for these tests utilized low speed flow at an operational Mach number of 0.06.

Henderson et.al and Greitzer [14, 15] identified the importance of component coupling in distorted flows. They demonstrated that a compressor would induce an irrotational velocity field ahead of it in response to the incoming distortion for low Mach number flows. This inviscid interaction would in turn have a strong impact on the rotor's lift, as the relative incidence angle and velocities have a first-order dependence on the circumferential velocity component at the fan face. Additionally, such induced velocity fields associated with the upstream distortion attenuation are related to the rotor's bound and shed vorticity.

Soeder and Bobula [20] measured the effect of steady state pressure distortion on inlet flow to a high-bypass ratio turbofan engine using circumferential distortion patterns tested at 80 and 90% of the design speed of 7000 RPM. Acquiring flow-angle, static pressure, and total pressure information regarding the distortion profile, they discovered that the yaw angle had the largest deviation between the distortion plane and inlet at the hub region. Also found was that static pressure distortion increased exponentially as flow approached the engine inlet, however the total pressure distribution displayed no axial variation between the distortion and engine inlet. The static and total pressure distortion was heavily attenuated between engine inlet and compressor exit.

Fidalgo et al. [16] performed a study on the NASA rotor 67 stage operating with a total pressure distortion covering a 120-deg sector of the inlet flowfield. Full-annulus, unsteady, three-dimensional CFD was used to simulate the test rig installation and the full fan assembly operating with inlet distortion. The local operating condition of the fan at different positions around the annulus was tracked and analyzed, and shown to be highly dependent on the swirl and mass flow redistribution that the rotor induced ahead of it due to the incoming distortion. The upstream flow effects led to a variation in work input that determined the distortion pattern seen downstream of the fan stage.

The upstream and downstream propagation of potential flow effects caused by the rotor has been studied. Falk et al. [28] investigated the unsteady-velocity field upstream of the single-stage axial fan in a F109 turbofan engine and found the three-component, unsteady velocity measurements at 1.0 fan-blade chords upstream of the fan face to be potential in nature, generated by the fan, and to propagate upstream at acoustic speeds into the engine inlet flow.

Kozak and Ng [29] demonstrated that IGV trailing edge blowing eliminates pressure and velocity deficits in the IGV wakes, reducing the viscous forcing function of upstream stators. Measurements were taken at 3.0 fan-chord lengths upstream of the fan face because 'upstream potential flow disturbance from the fan needed to be removed from the measurements.'

The effect of inlet flow distortions on jet-propulsion systems remains an active area of testing and research for engine evaluation and qualification for both modern and advanced engine-airframe configurations.

Presented Research

The work presented here includes an in-depth analysis of the flow development of a screen-produced total pressure distortion profile (Part I) and how the presence of the rotor downstream of the screen plane affects this development (Part II). Considered in detail for several profile development lengths are the radial and circumferential time-averaged total pressure measurements, the calculation of ARP1420 distortion indices, and the change in radial and circumferential gradients within the profile. Such an analysis that tracks the development of the distortion profile downstream of the screen plane have not been detailed in the literature and to this author's knowledge is the first such an analysis.

The goals of this research were (1) to obtain insight into the development of a total pressure distortion through a constant diameter duct and (2) provide an introductory analysis into the effects of distortion screen positioning with respect to the rotor. This study calls attention to screen-produced distortion effects not previously reported in the literature, in particular to the effects of development and screen/fan placement on the calculation of distortion descriptors. Recommendations will be made regarding screen positioning for ground-test distortion applications using actual engine components.

Chapter 2 - Experimental Design

To accomplish the goals of this research, an experimental setup and plan was designed to take advantage of the unique equipment available at the Virginia Tech Turbomachinery and Propulsion Laboratory. To study the flow development of the distortion profile in a constant diameter tunnel and the rotor impact on this profile, it was required to construct a variable length inlet duct, and a means to mount and vary the location of a distortion screen and total pressure measurement rake. To accomplish this, a series of constant diameter tunnel duct segments measuring one diameter in length were constructed. These tunnel 'sections' could be bolted together in series to produce the required tunnel length, with a maximum fan-to-inlet length of 11 duct diameters. By varying the number of tunnel sections connected, the overall length of the tunnel could be adjusted as needed. Also, these tunnel sections were constructed so as to interface with a total pressure rake array (TPRA). This allowed for a variable measurement plane, so that the flow development of the distortion profile could be captured by moving the TPRA sequentially downstream of the screen.

Physical Components used in Experiment

Turbofan Engine

To generate the flow through the duct and produce the rotor presence needed for the analysis of the fan/screen interaction, a modified Pratt and Whitney Canada (P&WC) JT15D-1 turbofan engine was used. The engine utilizes a two-spool design, housing a single stage axial flow low pressure compressor and one centrifugal flow high pressure compressor. The engine inlet diameter is 21 inches, with a bypass ratio of 3.3 and a maximum inlet mass flow of 75 lb_m/s at 16,000 RPM fan speed, producing approximately 2,200 lb_f-thrust. The engine was placed downstream of the test article and instrumentation providing a negative pressure differential in the duct, pulling air from outside the test cell and forcing it through the tunnel. A photograph of the engine is shown in Figure 4 with accompanying experimental test setup.

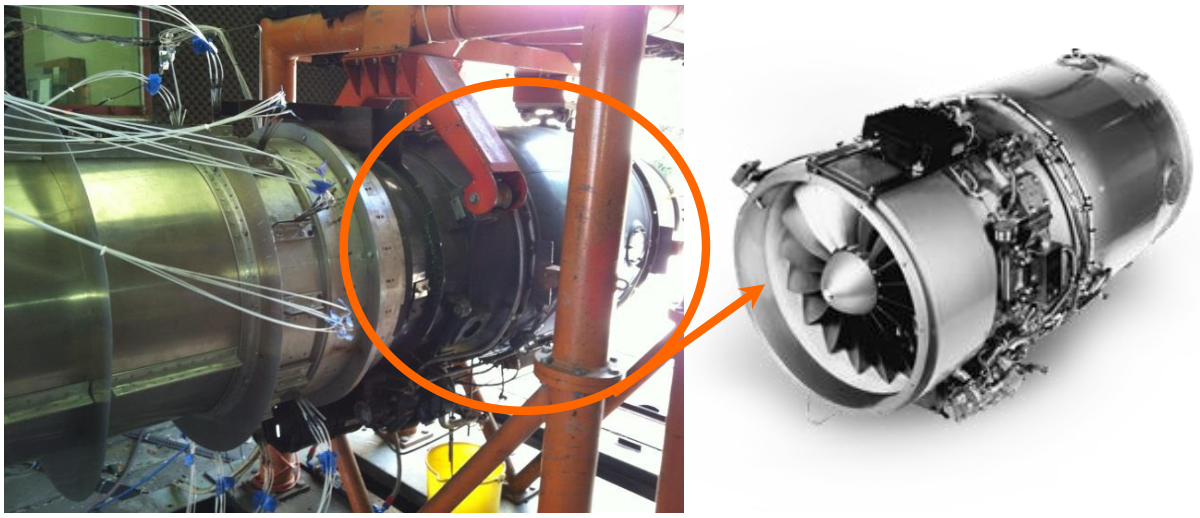

Figure 4. Typical engine mounting configuration (left, photo by Author, 2013) and P&WC JT15D-1 (right, [http://www.pwc.ca/files/images/engineFamily/vi_jt15d.png Accessed 2013/03/20, used under fair use, 2013]).

Distortion Screen

The distortion screens used for the experiments were supported by an 86.1% porosity backing grid mounted between two 20 gauge aluminum sheet metal sections that were riveted together to create a screen flange assembly. The backing screen alone was considered an "undistorted screen". The distortion screens had additional low porosity (77.5%) screen sections anchored to the backing grid. To generate the low recovery regions required by the profile, the low porosity sections were stacked in a cross-hatch fashion to produce the desired flow loss and distortion. These sections were attached to the backing grid using a waxed, nylon monofilament, with the outer edges of the sections coated with an ethylene-vinyl acetate (EVA) copolymer to prevent fraying. Photographs of the distorted and undistorted screens used in the experiments are shown in Figure 5.

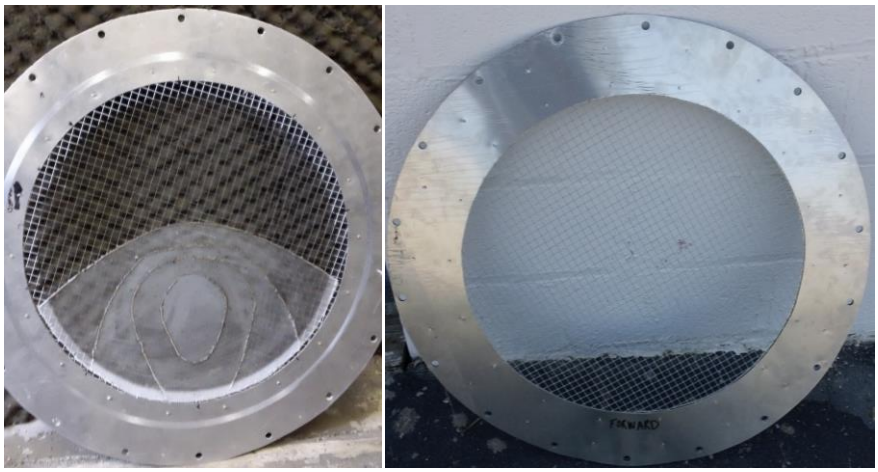

Figure 5. Distorted (left) and undistorted (right) screens used in the experiments. Photos by Author, 2013.

Distortion Screen Support and Inlet

To support the screen sections, it was necessary to construct a system that housed the screen in a vertical orientation and was capable of surviving the dynamic pressures from the incoming airflow. A large, 32" outside diameter slew-ring bearing was acquired and bolted to a support structure that held the bearing in an upright orientation. The bearing was a component of a rotation system for the screens (not used in this investigation). The distortion screen flange assemblies were machined with an accompanying bolt-hole pattern to connect directly to the back of the bearing, providing a secure fit. A photograph of the bearing system is shown in Figure 6.

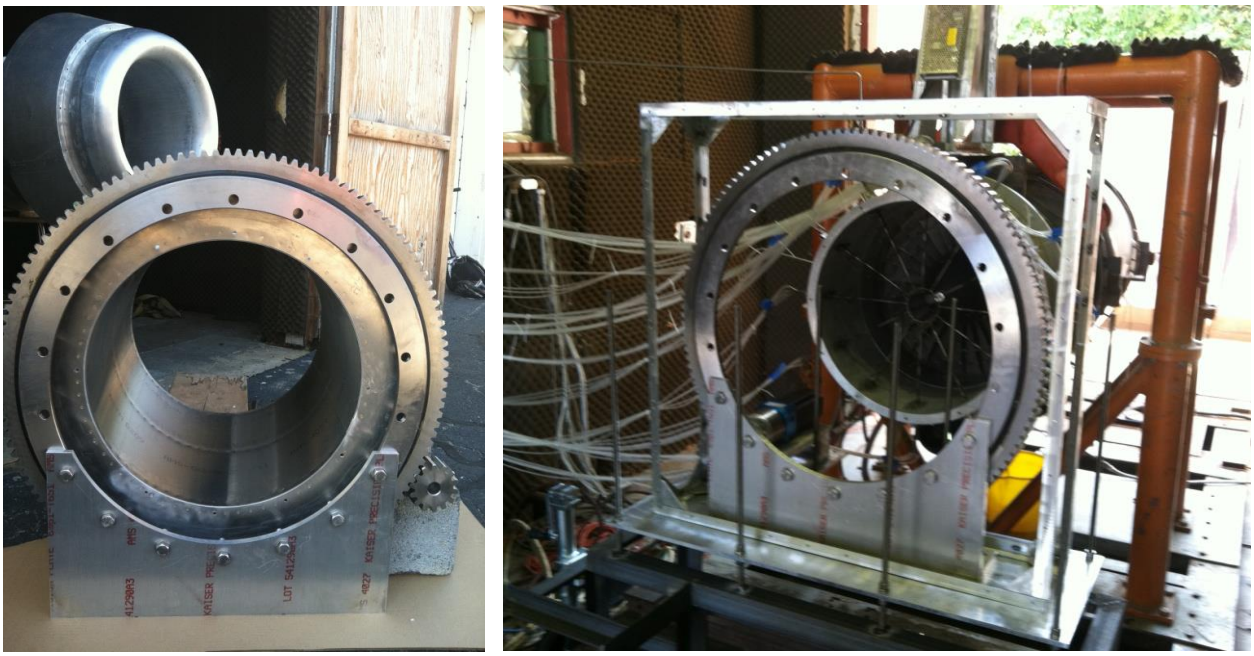

Figure 6. Photographs of distortion screen support rig and bearing (left), and support stand assembly (right). Photos by Author, 2013.

The bearing and its necessary support components were housed inside a sealed, transparent polycarbonate box that is shown in Figure 7. This box prevented any leakage of air into the tunnel. Two custom-built tunnel sections were inserted upstream and downstream of the bearing section to mate with the components inside the polycarbonate box. The box was sealed with aluminized tape applied to the junctions between the polycarbonate and aluminum tunnel sections. The downstream tunnel section incorporated a slip-ring design that allowed for rotation of the screen section. The upstream tunnel section was connected to an aerodynamic inlet, also shown in Figure 7. It was held at a fixed location, 1.43 diameters upstream of the screen plane for all reported experiments.

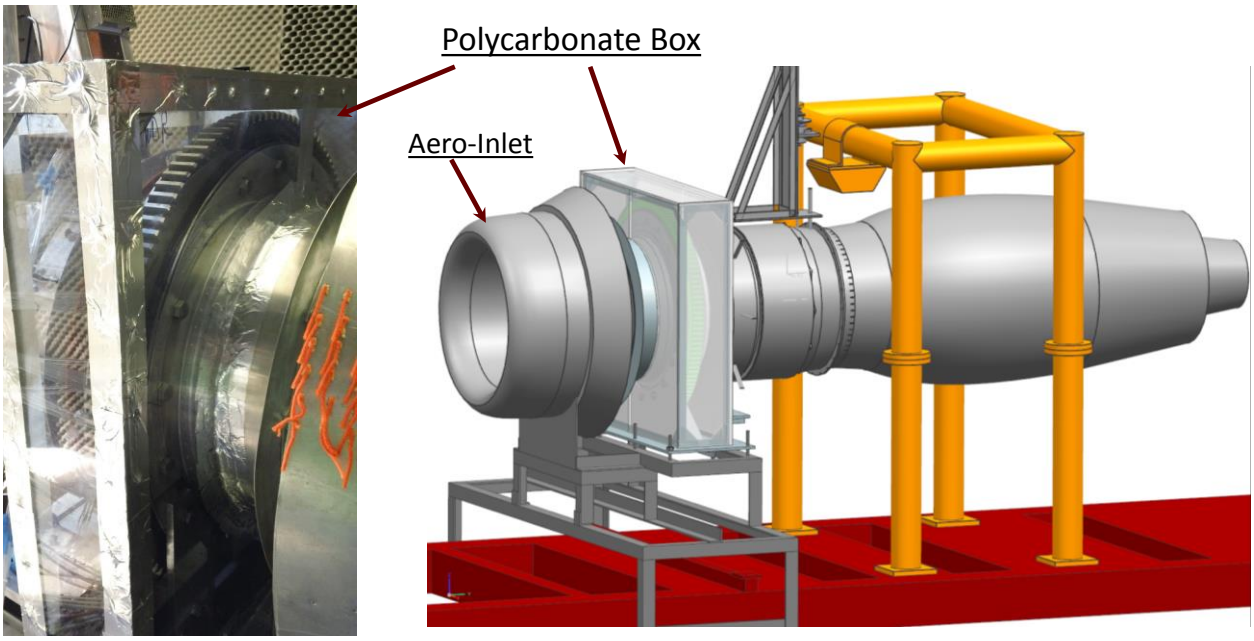

Figure 7. Photograph (by Author, 2013) and CAD model of distortion screen sealing chamber and aerodynamic inlet.

Variable Length Tunnel

To obtain the desired varying development lengths downstream of the screen plane, it was necessary to construct several tunnel sections that could be assembled in various combinations with the distortion screen support, the total pressure rake array (TPRA), and the engine. These sections were composed of 20 gauge aluminum sheet metal and 1x1x1/8" rolled aluminum angle that were riveted together to compose connecting sections one diameter in length.

For extended length tests when up to 10 duct diameters were required between the distortion screen and fan face, it was necessary to independently support the sections, but also to allow them to move axially with the expansion of the engine during testing. Support frames were constructed from low carbon steel angle that utilized a turnbuckle suspension system. Shown in Figure 8 is a photograph of the final assembly of the tunnel sections and support structure. Trailer jacks were also attached to the side of the frame, as was done with the inlet/bearing support stand.

Figure 8. Tunnel section turnbuckle support system. Photos by Author, 2013.

Screen-Produced Distortion Pattern

The selected screen-produced profile used in this research was designed to simulate the distortion generated by a serpentine BLI inlet. As shown in Figure 9-left, the desired flow profile is a circumferentially-dominated, vertically symmetric total pressure distortion. In the left and right profiles shown in Figure 9, red is indicative of a high local total pressure and blue indicates low total pressure. Following in a clockwise fashion around the profile face, the "12 o'clock" position at the top of the profile occupies an expansive high total pressure region, with a significantly reduced total pressure from the "3 o'clock" to "5 o'clock" positions, and the minimum total pressure region at the "6 o'clock" position. The low total pressure region of the profile encompasses a circumferential arc from "4 o'clock" to "8 o'clock".

The fabricated screen produced an acceptable representation of a BLI serpentine inlet, capturing the low total pressure region at the bottom and the circumferential distortion extent and intensity of the high total pressure region at the top of the annulus. The resulting screen profile at 0.28 duct diameters downstream of the screen plane is shown Figure 9-right.

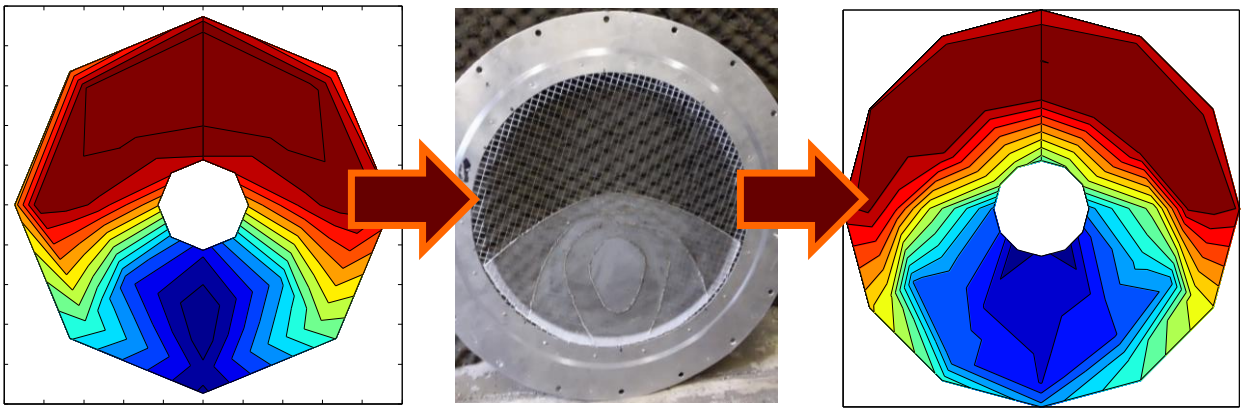

Figure 9. Desired profile (left), distortion screen (center, photo by Author, 2013), and simulated (right) distortion profiles.

Experimental Investigations

Having the necessary components to complete the experiment, a series of tests were performed to obtain the data required to document the flow profile development in the absence and in the presence of the fan. This was accomplished by first placing the screen plane sufficiently far upstream of any fan influence, and then moving the measurement plane to several locations downstream of the screen plane to track the development of the profile. This experimental procedure comprised Part I of the study. In Part II, the fan effects on distortion profile development were studied by moving the screen plane closer to the fan face. The development lengths established in Part I of the study were preserved in Part II, and the screen was placed close enough to the fan to produce a change in profile development. The similarity of the flow between test cases was maintained by matching corrected flow conditions, and the engine speed was monitored using tachometers on the engine control panel. Ambient conditions were monitored using the barometer and thermometer employed by the local airport, which was located approximately 500 feet from the test facility.

Test Parameters

Test Configurations for Studying Profile Development (Part I)

To measure the development of the distortion profile as it traversed the tunnel, it was necessary to minimize the interaction between the screen and fan. To accomplish this, the screen was placed at the maximum allowable distance from the fan face given the amount of individual tunnel sections constructed. For Part I of this research, the screen plane was located at a fixed position of 9.65 duct diameters in front of the fan and the Total Pressure Rake Array (TPRA) at the measurement plane was moved downstream of the screen plane for varying development lengths. Shown in Figure 10 is an illustration of the test progression, with the measurement plane moved to varying development lengths (A) downstream of the fixed screen plane.

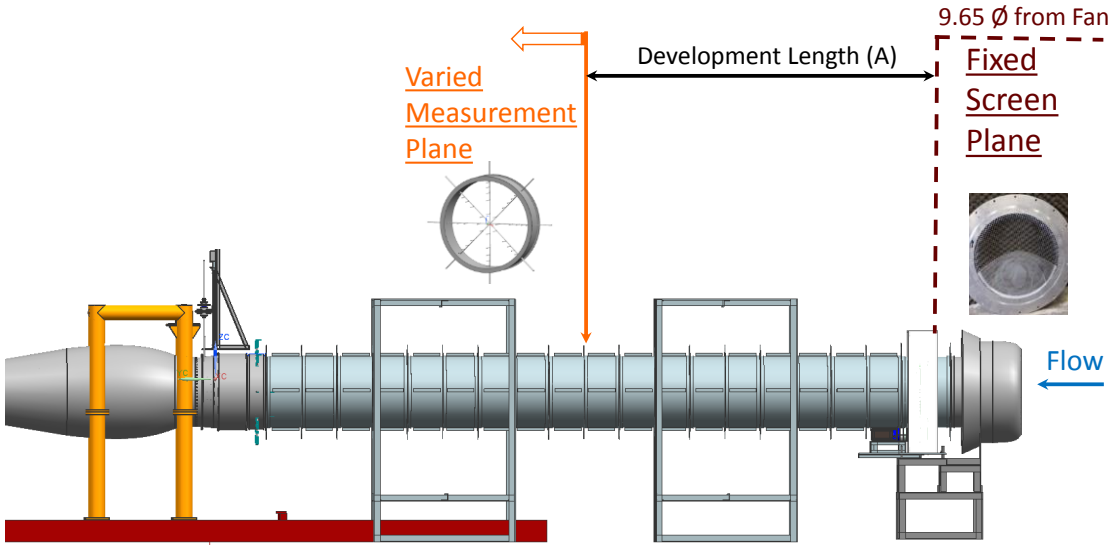

Figure 10. CAD model showing TPRA measurement plane variation in relation to fixed screen plane.

The measurement plane locations utilized for Part I correspond to 0.28, 1.0, 2.0, 5.0, and 9.0 duct diameters behind the screen plane, providing 0.28, 1.0, 2.0, 5.0, and 9.0 duct diameter development lengths.

The test progression is illustrated in Figure 11 and tabulated in Table 1. This 'Long' tunnel configuration allowed the distortion profiles to be studied with minimum effect of the fan on the screen-generated profile development.

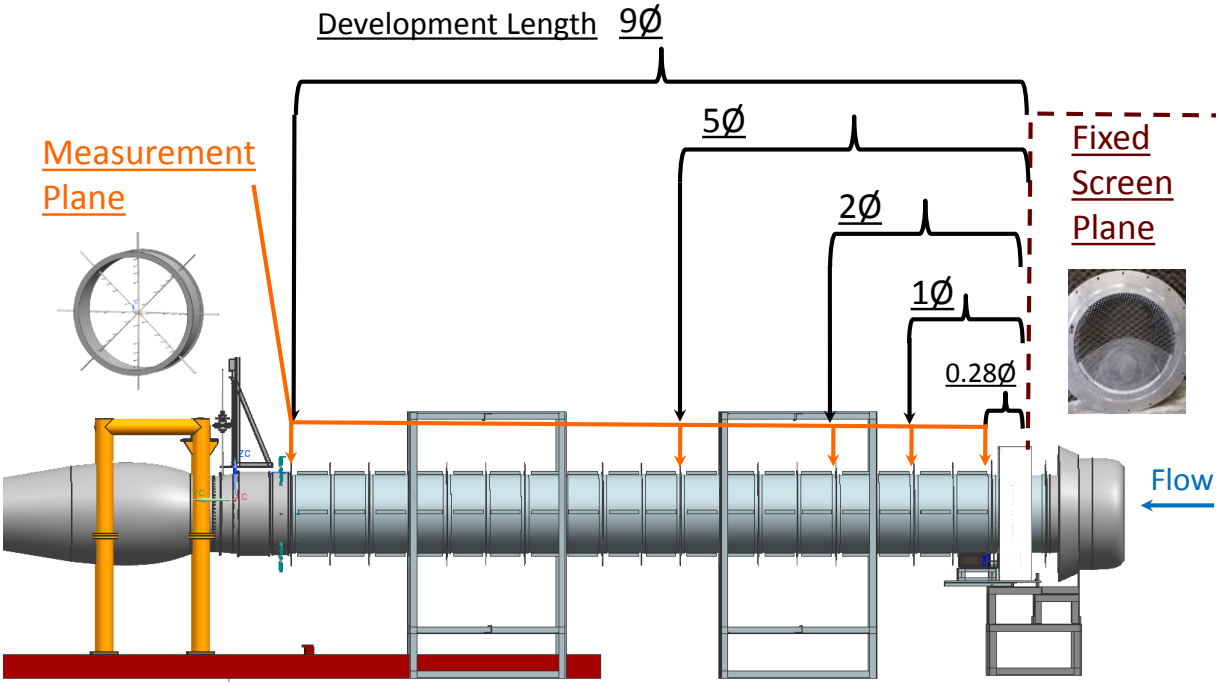

Figure 11. CAD model showing TPRA measurement plane locations for profile development study.

Table 1. Part I screen plane and measurement plane locations.

Part I - Distortion profile development, distances given in tunnel diameters, 1.0Ø=21"			
Development Length	Fan Face to Measurement Plane	Fan Face to Screen Plane	Screen Plane to Measurement Plane
0.28	9.37	9.65	0.28
1	8.66	9.65	0.99
2	7.66	9.65	1.99
5	4.66	9.65	4.99
9	0.66	9.65	8.99

Test Configurations for Studying Fan/Screen Interaction (Part II)

Part II of this study was designed to investigate the influence of the fan presence on the development of the distortion profile. This was accomplished by fixing the measurement plane 0.66 duct diameters in front of the fan face and moving the screen plane closer to the fan. The test progression is shown in Figure 12, with the development length (A') decreased from 9 to 0.28 duct diameters. The full test suite is illustrated in Figure 13.

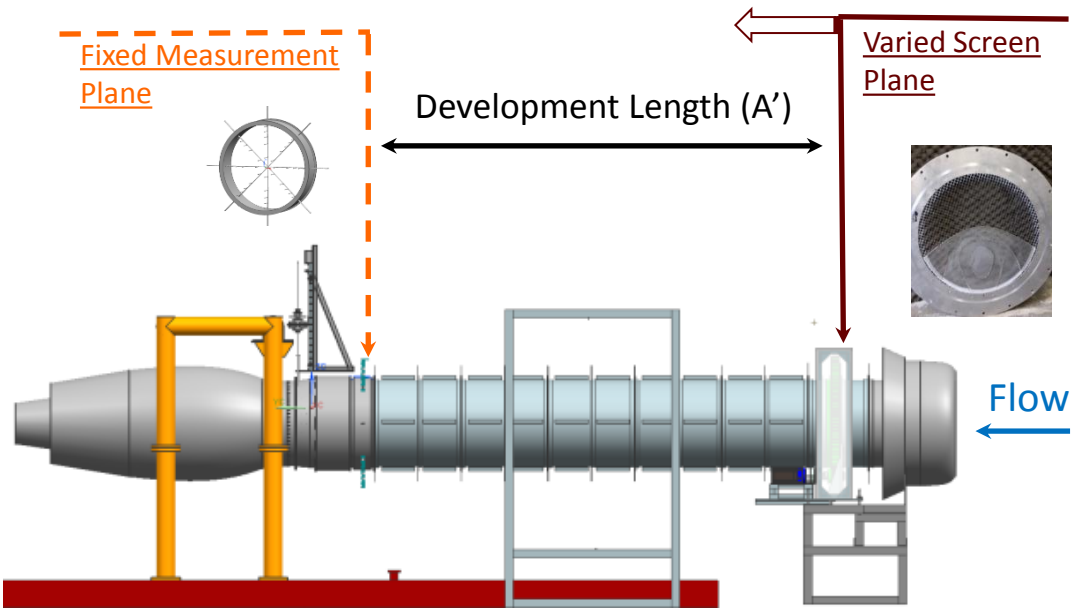

Figure 12. CAD model showing varying screen plane positions relative to fixed measurement plane.

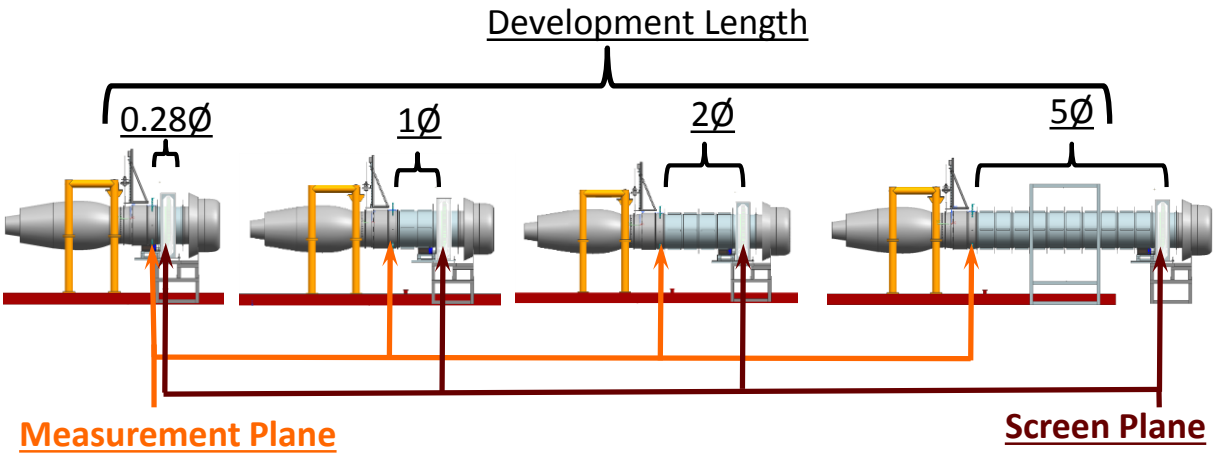

Figure 13. CAD model showing screen plane and measurement plane configurations for Part II.

To compare the distortion profile development obtained in Part II to that measured in Part I, the development lengths between the screen and measurement plane had to be preserved. Figure 14 shows an illustration comparing the two testing configurations. For Part I, the screen plane was fixed far enough upstream of the fan face so that the development could be assumed to be unaffected by its presence. In Part II, an investigation into the altered flow development is conducted by placing the screen in closer proximity to the fan face. Therefore, the development lengths studied in Part I (5, 2, 1, and 0.28 duct diameters) were duplicated in Part II with the exception that the screen was placed at sequential locations closer to the fan while still preserving these development lengths. Referencing Figure 14, in Part II the measurement plane was fixed at 0.66 diameters in front of the fan and the screen was moved closer to the fan, with the constraint A' = A , or the development length from the screen plane to the measurement plane between Parts I and II remained equal. Part II testing configurations are referred to as the 'Short' tunnel, with the configurations given in Figure 11 referred to as the 'Long' tunnel. This terminology is used in the remainder of the thesis

to distinguish between the two tests. Table 2 compares the screen and measurement plane locations for Parts I (long tunnel) and Parts II (short tunnel).

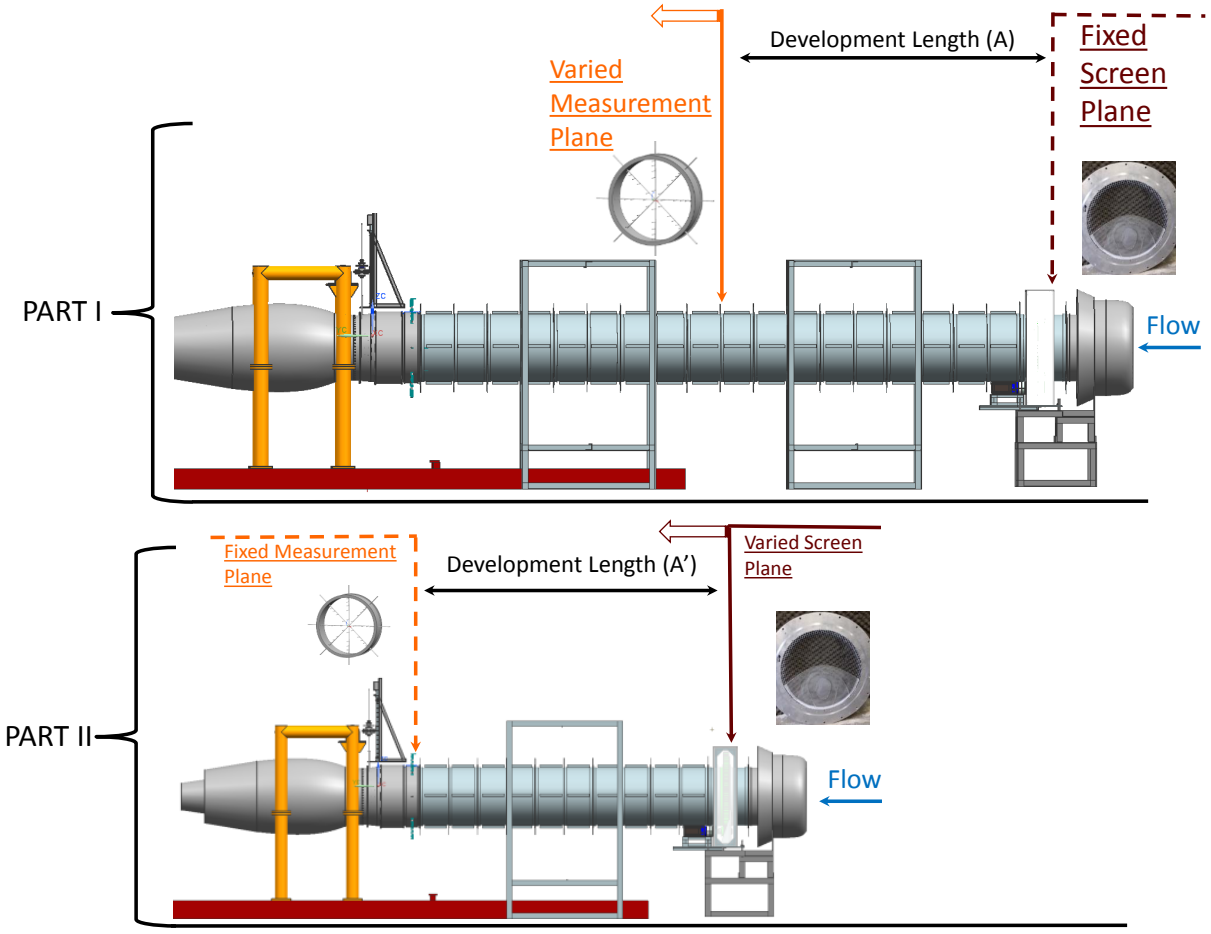

Figure 14. CAD model showing tunnel configurations for Parts I and II. Development length preserved with A=A'.

Table 2. Part II screen plane and measurement plane locations.

Part IIb - Fan/Screen interaction, distances given in duct diameters 1.0Ø=21"		
0.28Ø development length		
	Part II - Short	Part I - Long
Screen plane to measurement plane	0.28	0.28
Screen plane to fan face	0.94	9.65
1Ø development length		
	Part II - Short	Part I - Long
Screen plane to measurement plane	0.99	0.99
Screen plane to fan face	1.65	9.65
2Ø development length		
	Part II - Short	Part I - Long
Screen plane to measurement plane	1.99	1.99
Screen plane to fan face	2.65	9.65
5Ø development length		
	Part II - Short	Part I - Long
Screen plane to measurement plane	4.99	4.99
Screen plane to fan face	5.65	9.65

Maintaining Equal Speed Cases

All reported results were obtained at 73% corrected fan speed, resulting in a corrected fan tip Mach number of 0.95 at approximately 11,680 RPM. The corrected fan speed is a percentage of the maximum rated speed of 16,000 RPM. This reduced speed was selected as the primary test condition, because for the closest fan/screen configuration the resulting distortion intensity was the highest the engine was able to safely handle.

Lower speed studies were also performed. Reducing the fan speed reduced the duct flow velocity, resulting in a reduced distortion intensity. Details regarding the lower speed results can be obtained from the author.

Chapter 3 - Experimental Methodology

Once the experimental design had been established and the necessary test articles and components constructed, appropriate instrumentation was needed to measure and record the total pressure profiles. Software was also written to collect, import, and view the data in an understandable format. The instrumentation, data acquisition system, and data processing techniques are described in the following sections.

Instrumentation

To measure the total pressure profile produced by the screen, it was necessary to construct a total pressure rake array (TPRA) that could be mounted in several locations along the length of the tunnel and record an adequate number of total pressures to describe the profile behavior. The specifics of the TPRA and its construction are explained in further detail in the following subsection.

Total Pressure Rake Array

The Society of Automotive Engineers Aerospace Recommended Practice ARP 1420 provides a technique for measuring and quantifying distortion intensities at the aerodynamic interface plane (AIP) and the effect on fan and compressor stall margin [22]. The AIP is an arbitrary location determined by the investigators and can be designated at any location upstream of the fan face. For this study, the different development lengths investigated produced varying AIP locations. Thus an AIP is not established or referred to, rather a ‘measurement plane’ is the designated terminology utilized. Using the varying development lengths given in the study, an AIP can be established depending on experimental needs.

Following the ARP1420 recommended practice, twelve rakes of five total pressure measurement probes each were arranged at 30-degree intervals around the measurement plane. Each rake measured the total pressure at the mid-radius of five equal-area rings, as shown in the images of Figure 15. The layout of the probes is shown in Figure 15-right. Flexible tubing was connected to the probe ends exiting the rake case and routed to pressure transducers used to measure the oncoming flow. The probes were sealed within the rake case using a RTV silicone bonding agent, and any excess was removed until the sealant was flush with the inner diameter of the rake case.

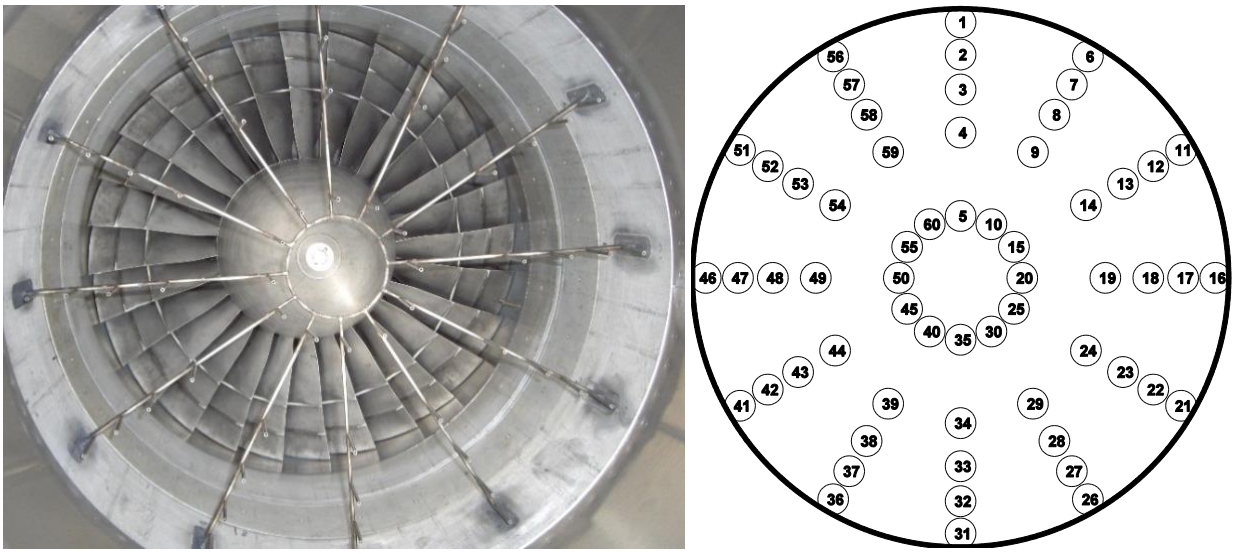

Figure 15. TPRA (left, photo by Author, 2013) and measurement location diagram (right).

Data Acquisition

The pressure lines originating from the outlet of the total pressure probes in the TPRA were routed to Omega PX139 5psi differential pressure transducers mounted inside the control room. All measurements made with the transducers were relative to atmospheric pressure (gauge pressure). The output signals from each transducer were connected to NI-6259 data acquisition cards. The data signal was processed by these cards and recorded via a computer. All transducers were sampled at 256 Hz using a multiplexing sampling technique. Pictures of the transducer layout and data acquisition system used are shown in Figure 16.

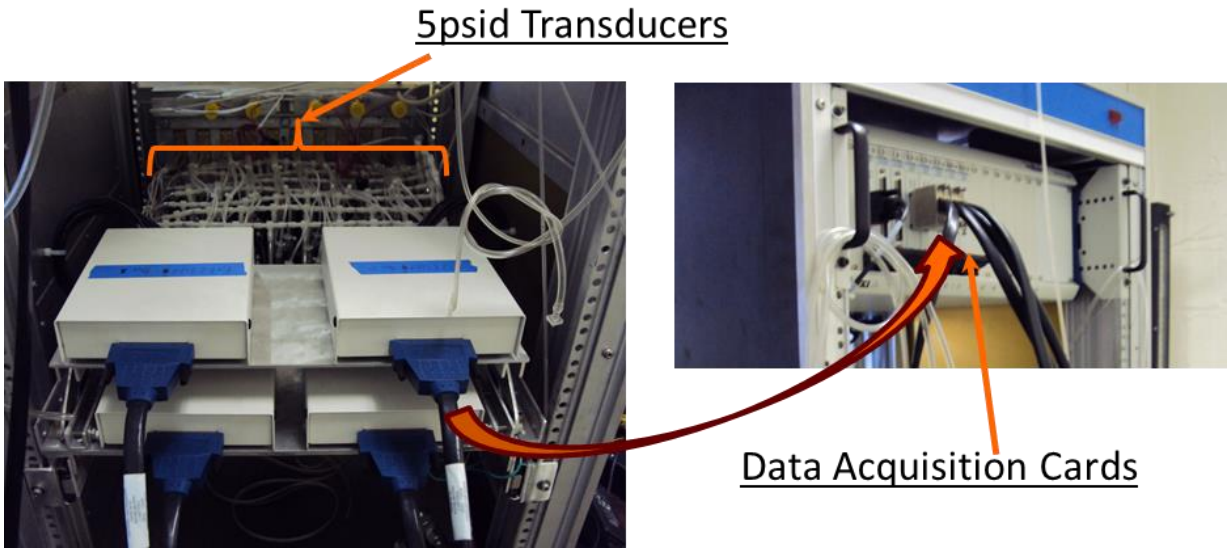

Figure 16. Pressure transducers and data acquisition cards used during experiments. Photos by Author, 2013

Shown in Figure 17 is a plot collection detailing the noise inherent in the data acquisition system. This data was obtained for a case of no inlet flow into the pressure probe. In the left column of Figure 17 is a plot of the mean zero signal over the course of a 60 second collection sampled at 256 Hz .The top-left plot

shows the noise inherent in the analog input signal, which contains contributions from both the transducer and the analog-to-digital (A/D) converter, as shown in Equation 1.

$$\sigma_{analog}^2 = \sigma_{transducer}^2 + \sigma_{A/D}^2 \quad (1)$$

The blue line is the analog noise and the black line is the least significant bit (LSB) in the A/D converter. The bottom-left plot shows the mean zero data of just the A/D converter shown in red and the LSB shown in black. This data was obtained by shorting the inputs to the A/D convertor and recording the signal for 60 seconds at a sampling frequency of 256 Hz. As shown from the left-column plots of Figure 17, the noise inherent in the system is quite low and is comparable to the LSB in the A/D converter. The top-right plot of Figure 17 shows a histogram of the mean zero analog data, indicating a normal distribution of the signal variation. A histogram of the A/D converter noise is shown in the bottom-right plot of Figure 17. The variation in the recorded pressure during the tests will be a contribution of both the analog input and flow fluctuations such that the total variance in the measured signal will follow Equation 2. As demonstrated in Figure 17, any variation observed in the signal will have the largest contribution from the flow fluctuations, not the data acquisition system.

$$\sigma_{signal}^2 = \sigma_{analog}^2 + \sigma_{flow}^2 = \sigma_{transducer}^2 + \sigma_{A/D}^2 + \sigma_{flow}^2 \quad (2)$$

The signal-to-noise ratio for the data was calculated to be approximately 50, following the formula given in Equation 3, where $\bar{x}$ is the sample mean and s is the sample standard deviation.

$$SNR = \frac{\bar{x}}{s} \quad (3)$$

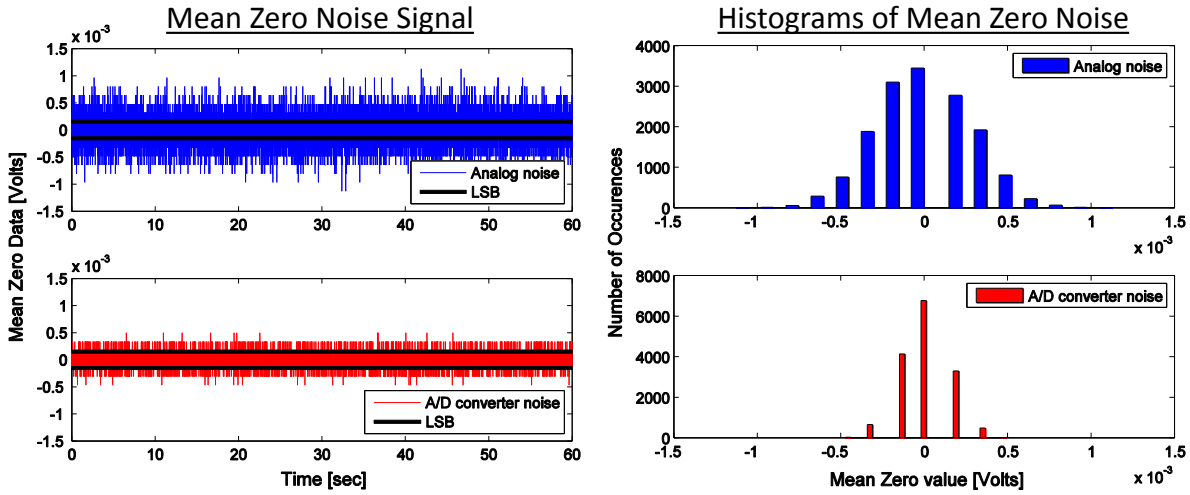

Figure 17. Mean zero (left column) and histogram (right column) plots of noise inherent in A/D converter and analog input signal.

Total Pressure Response

The response time of the pressure transducers was calculated by supplying a pressure driven step input and measuring the settle time of the transducer response. This was accomplished by inserting a computer controlled valve upstream of the transducer pressure line. Pressure from a compressed nitrogen tank was

regulated down upstream of the valve and opened to allow air flow through the pressure line into the transducer. Both the valve and pressure transducer response were recorded on the NI acquisition cards. The length of the pressure line for the first test was 6", with the second and third test hose length increased to 25', corresponding to the length travelling from the transducer to the TPRA. The input pressure for the first and second tests was 2.787 psi to determine the response for a 'high' input pressure to the transducer. The pressure for the third test was lowered to 0.202 psi to mimic testing conditions where only small changes in the incoming pressure were of interest. An illustration of the test setup is shown in Figure 18.

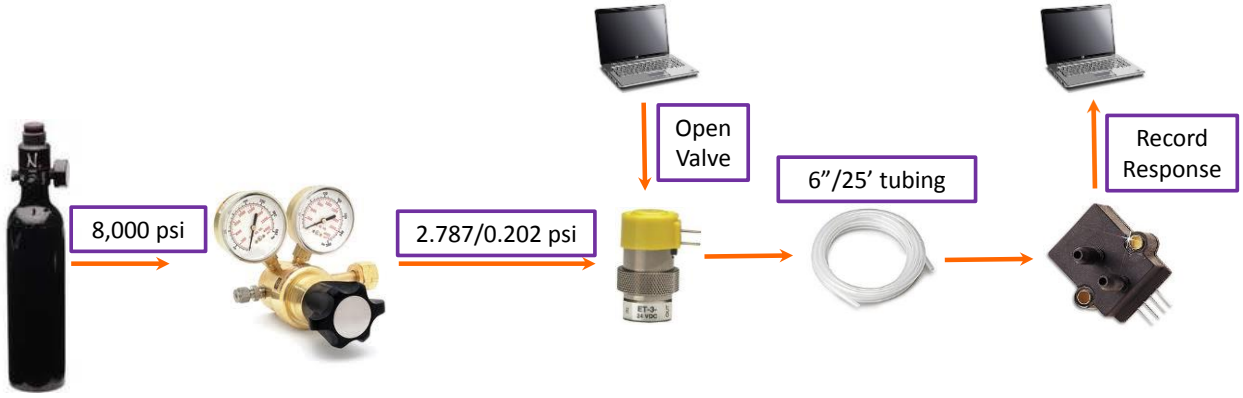

Figure 18. Experimental setup to measure response time of pressure system.

Results from the test are shown in Figure 19. The top plot shows the time-resolved results of the recorded signal. The valve control is shown in green, with the transducer response shown in blue, red, and black for varying hose lengths and input pressures. The test specifics are given in the legend in the lower right-hand corner. It is shown that the settle time of the system is increased for increased hose length and decreased input pressure. For the actual experimental measurements, the black line is representative of the expected response of the system. The use of the long pressure hose between the transducer and the TPRA acts as a low-pass filter, limiting the frequency content in the flow that can be captured by the transducers. The bottom plot of Figure 19 shows the frequency-resolved content of the three test cases. The color designation for the three curves follows that given in the time-domain plot. The resulting frequency curves resemble a sine function (Fourier transform of a rectangular pulse in the time-domain), with the amplitude of the decaying sinusoid severely reduced and the zero-crossing frequency increased for increased tube length, and decreased for a lower input pressure step. The results of this analysis show the incoming flow parameters are filtered via the long pressure line between the TPRA and transducer, reducing the measurable frequency content of the flow variation to less than or equal to 1 Hz.

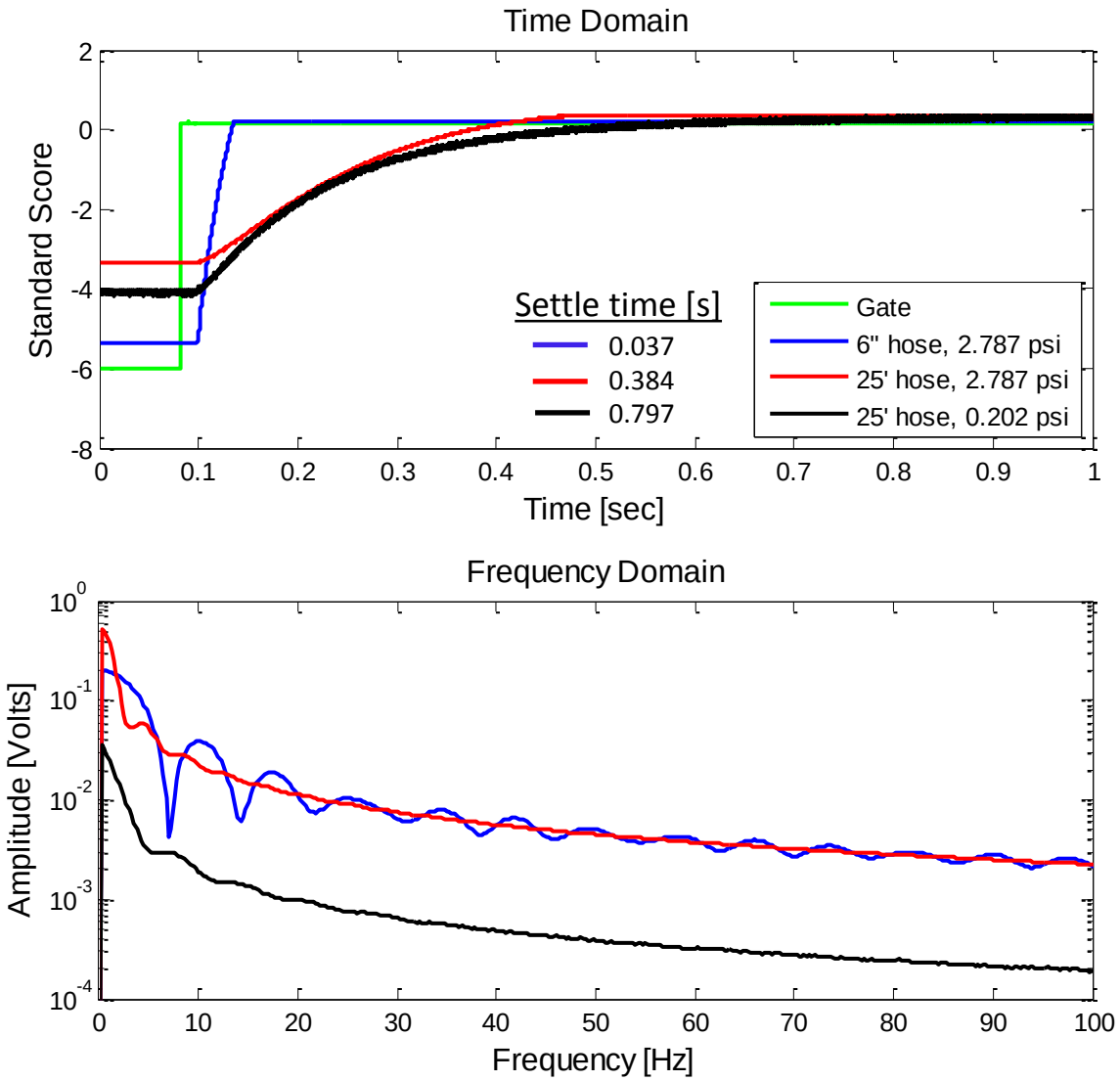

Figure 19. Time domain (top) and frequency domain (bottom) response of pressure transducer with increasing hose length.

Data Calibration and Uncertainty

All transducers were calibrated at the conclusion of each test according to manufacturer specifications and Virginia Tech Turbomachinery laboratory standards, establishing the relationship between pressure and voltage. The uncertainty for each measurement was calculated and is given in detail in the Appendix.

Data Processing

To eloquently present the data, several post processing techniques were utilized. They include standard statistical analysis and calculations recommended by ARP1420 for processing total pressure rake data. The processing techniques are presented in the following subsections.

ARP1420-Based Analysis

The Aerodynamic Recommended Practice (ARP) for the processing of total pressure distortion data sets is summarized in the document ARP1420 [22]. The purpose of this guideline is to provide methods for consistently evaluating gas turbine engine compressor aerodynamic stability and performance, as affected by the quality of the airflow delivered to the engine. Of particular note for this study is the calculation of three distortion parameters; circumferential intensity, circumferential extent, and radial intensity. Shown in Figure 20-left is a graphic of the distortion descriptors used in the analysis. PAV_i (ring average pressure) and $PAVLOW_i$ (average low pressure) are defined by Equations 3 and 4 respectively, and the circumferential distortion extent and intensity is defined by Equations 5 and 6, respectively.

$$PAV_i = \frac{1}{360}\int_0^{360} P(\theta)_i d\theta \quad (3)$$

$$PAVLOW_i = \frac{1}{\theta_i}\int_{\theta_{1_i}}^{\theta_{2_i}} P(\theta)_i d\theta \quad (4)$$

$$Extent: \theta_i^- = \theta_{2_i} - \theta_{1_i} \quad (5)$$

$$Circumferential\ Intensity: \left(\frac{\Delta PC}{P}\right)_i = \left(\frac{PAV - PAVLOW}{PAV}\right)_i \quad (6)$$

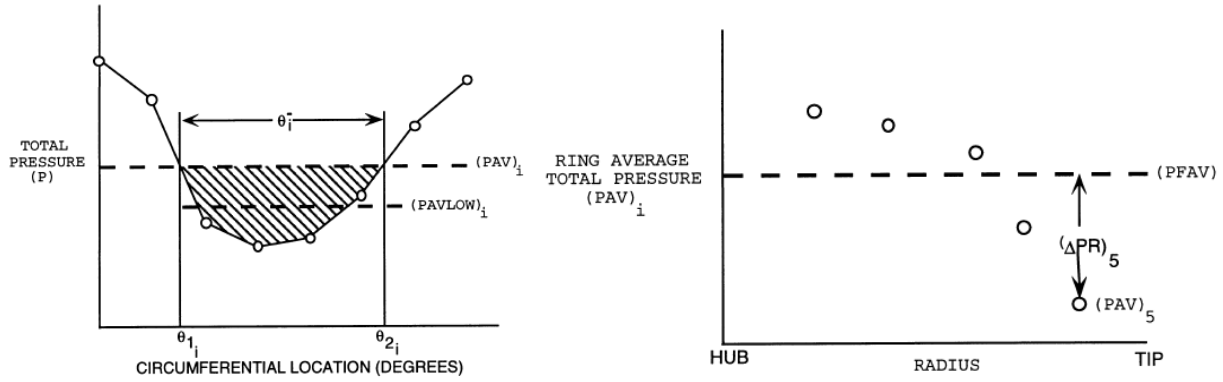

Figure 20. Ring circumferential distortion for a once-per-revolution circumferential distortion (left) and typical radial distortion pattern (right) [22].

Circumferential intensity is a relative comparison of the circumferential pressure to the low pressure region for each radius, indicating the magnitude of the average circumferential pressure with respect to the deficit region. A higher value indicates a higher discrepancy or more intense distortion region. Circumferential extent is the circumferential duration of the pressure region that is below the average pressure at a given radius.

The radial distortion intensity is defined in Equation 7 and an example of the results for a distortion pattern is shown graphically in Figure 20-right. The distortion parameter PFAV (area weighted face average pressure) used in the calculation of radial distortion intensity is defined in Equation 8.

$$Radial\ Intensity: \left(\frac{\Delta PR}{P}\right)_i = \left(\frac{PFAV - PAV_i}{PFAV}\right)_i \quad (7)$$

$$PFAV = \frac{1}{N}\sum_{i=1}^{N} PAV_i \quad (8)$$

Pressure Recovery

Unless otherwise noted, the data was processed and presented as a pressure coefficient termed 'Recovery', which is defined in Equation 9. Recovery is a normalization of the local pressure to the referenced atmospheric pressure, thus high total pressure and high recovery are synonymous. An alternative method of viewing the data is as a 'Loss' parameter, defined in Equation 10. Both coefficients convey equivalent meanings regarding the results, either a fraction of the initial total pressure ('Recovery') or a fraction of the encountered losses ('Loss'). 'Recovery' is used as the defining parameter for all analyses presented in the following sections.

$$Recovery = \frac{P}{P_{atm}} \quad (9)$$

$$Loss = 1 - \frac{P}{P_{atm}} = 1 - Recovery \quad (10)$$

Tunnel Condition Estimations

For the results given in Chapters 4 and 5, it was advantageous to determine flow conditions within the tunnel by estimating the Reynolds number and developed boundary layer thickness. Given in the following subsections is an analysis showing how these estimations were derived.

Tunnel Flow Velocity

The tunnel configurations used for the experiments did not contain a mass flow calibrated inlet and therefore it was not possible to accurately calculate the tunnel flow velocity. The flow velocity can be estimated however using known engine performance data for the JT15D-1 and interpolating the approximate mass flow for the given operating fan speed [27]. Shown in Figure 21-left is the relationship between fan speed and mass flow rate for the engine. Interpolating the curve for 73% fan speed as shown, the mass flow rate through the tunnel can be estimated as 51 lbs/sec. While the implementation of the distortion screen reduces the effective tunnel diameter and will correspondingly reduce the mass flow rate through the tunnel, this is considered to be a valid estimation procedure.

Following the mass flow rate estimation from Figure 21-left, the tunnel velocity can be estimated using Equation 11 for a compressible, ideal gas.

$$\dot{m} = AP_0\sqrt{\frac{\gamma}{RT_0}}M\left(1 + \frac{\gamma - 1}{2}M^2\right)^{-\frac{\gamma+1}{2(\gamma-1)}} \quad (11)$$

Also understood using this equation is the effect of reduced tunnel area as a result of the presence of the distortion screen. Although the reduced area of the distortion screen will create a nozzling effect within the tunnel and effectively accelerate the velocity of the flow through the screen, this was a highly localized phenomena restricted to close regions upstream and downstream of the screen and not captured within the TPRA.

Using compressible, isentropic flow relations given in Equations 12 and 13, the tunnel velocity can be calculated via Equation 14 and was determined to be 87.9 m/s, at a Mach number equal to 0.26.

$$\frac{T_0}{T} = 1 + \frac{\gamma - 1}{2} M^2 \qquad (12)$$

$$M = \frac{u}{\sqrt{\gamma R T}} \qquad (13)$$

$$u = M \sqrt{\frac{\gamma R T_0}{1 + \frac{\gamma - 1}{2} M^2}} \qquad (14)$$

Internal Flow Conditions

To establish flow conditions within the tunnel, the Reynolds number for flow in a pipe can be calculated using Equation 15.

$$Re_D = \frac{uD}{\nu} \qquad (15)$$

Referencing standard atmospheric conditions at a temperature of 288.15K to estimate the kinematic velocity, ν, the pipe Reynolds number was estimated to be 3.2×10^6, which is much greater than the critical Reynolds number of 4000, confirming that the flow in the tunnel is indeed turbulent.

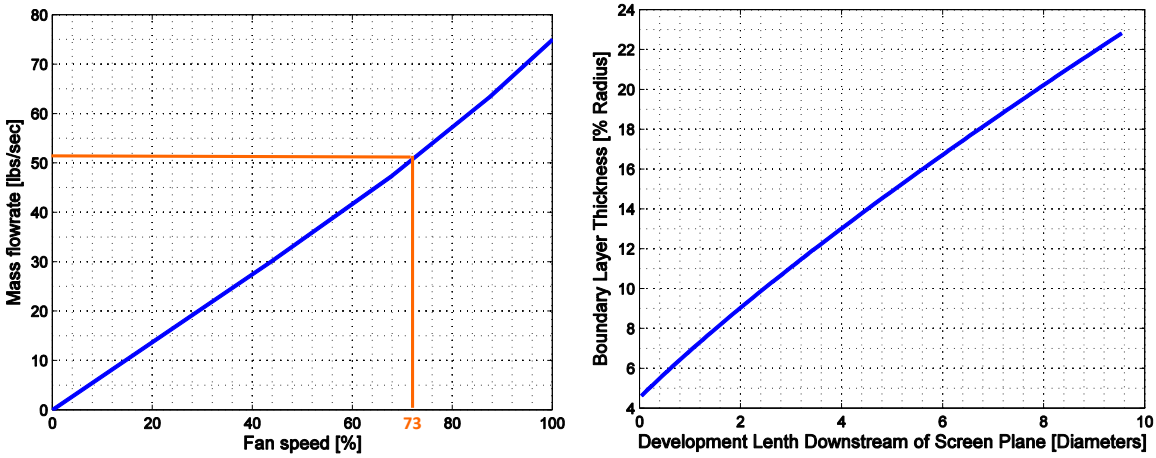

Figure 21. Mass flow rate vs. fan speed curve (left) and boundary layer thickness estimation.

Boundary Layer Height

The boundary layer thickness within the tunnel, an important characteristic of the flow that becomes more prevalent for increased development lengths, can be estimated using the equations derived for flow

over a flat plate. The turbulent transition point is calculated using Equation 16, and using the tunnel velocity estimated from the previous subsection, referencing standard temperature, and evaluating for a critical transition Reynolds number, $Re_{cr} = 5x10^5$, the critical streamwise distance is estimated as 0.155 duct diameters [26].

$$x_{cr} = \frac{\nu Re_{cr}}{u} \quad (16)$$

It is therefore valid to conclude that a turbulent boundary layer flow regime exists at all measurement planes within the tunnel. Using Equation 17 to calculate the Reynolds number at a specific development length downstream of the screen, the boundary layer height can be estimated using Equation 18 [26].

$$Re_x = \frac{ux}{\nu} \quad (17)$$

$$\delta = \frac{0.370x}{Re_x^{1/5}} \quad (18)$$

Shown in Figure 21-right is an estimation of the boundary layer height in percent radius from the tunnel wall for increasing development length downstream of the screen plane. The boundary layer has an initial height immediately downstream of the screen plane to account for the inlet length prior to the screen. As shown, the boundary layer height becomes quite substantial after 9 duct diameters of development, reaching approximately 22% of the tunnel radius, creating a significant blockage within the tunnel leading into the fan.

Chapter 4 - Results

Tunnel Validation

To provide a method for consistent reporting of the flow conditions in the tunnel, it was necessary to perform an analysis on the effect of variation in fan speed over the course of a data collection, and also to validate the uniformity of the tunnel using a series of undistorted screens.

Quasi-steady Inlet Conditions

The fuel control unit (FCU) on the engine utilized two input pressure lines bled from the core and bypass outlets to control the fuel flow rate. Normal unsteadiness of the bypass and core outlet pressures changed the amount of fuel used and produced a constantly varying fan and core speed for the duration of each test.

Figure 22 is a series of plots for four tunnel configurations showing a RPM trace during the course of a five-minute data collection. The respective titles of each subplot represent the tunnel length, from the fan face to the inlet entrance. A once-per-rev sensor was utilized to accurately determine the rotational speed of the fan. This sensor was sampled at 150 kHz and a RPM trace was determined by averaging the calculated rpm every 0.25 seconds. Thus for a 300 second collection, a record of 1200 samples was created. The plots below show an approximate +/-60 rpm (+/- 0.5%) variation in fan rotational speed over the course of the test. As a result of this variation, five minute collection times were used for all test cases to ensure the collection of a statistically representative data set. This allowed the calculation of a time-average that did not significantly change over the course of the collection.

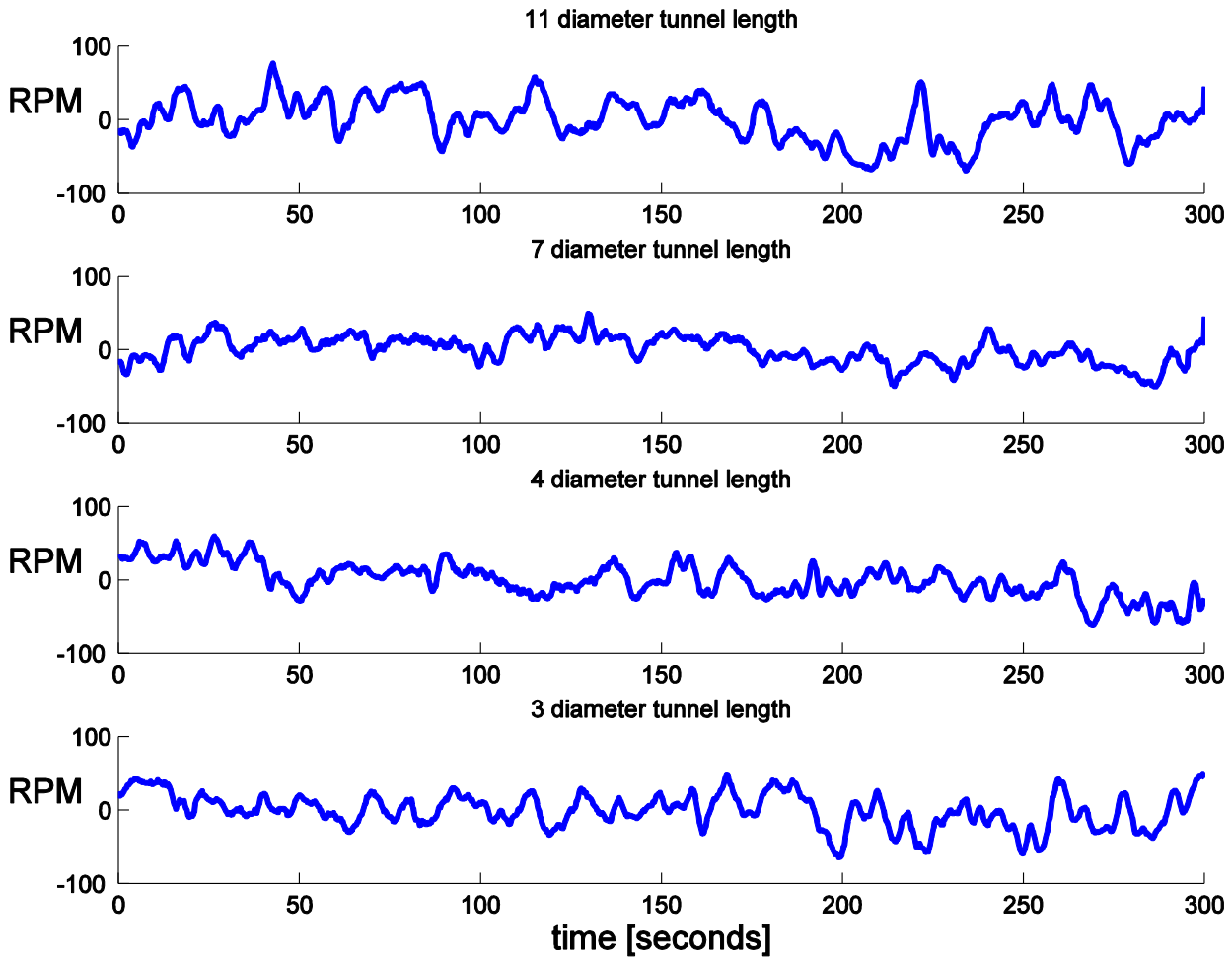

Figure 22. RPM trace of several engine/inlet configurations.

Tunnel Uniformity

Shown in Figure 23 is a sample of the results of undistorted tests performed to verify the uniformity of the tunnel. Each contour subplot represents a different development length increasing from right (0.28 duct diameters) to left (9 duct diameters). The title of each subplot indicates the development length of the distortion profile and the arrows indicate the position of the measurement plane in the tunnel. These tests were performed under equivalent operating and acquisition conditions as the distorted cases, but using the undistorted backing grid only. As shown in Figure 23, the highest recovery region is centralized within the center of the annulus and exhibits a radial distortion on the outer edge where a significant boundary layer develops in the tunnel. This is most evident for 9 diameters of profile development.

Figure 24 shows plots of boundary layer development in further detail for the twelve circumferential measurement sets taken with the TPRA. For Figure 24 and subsequent similar graphs, the locations relative to the outer wall of the duct are plotted on the ordinate to produce a boundary layer – like presentation of the results. As expected, higher losses occur for increased development lengths across the entire radius and the results are consistent for each circumferential location around the annulus.

Of important note in Figure 23 is the development of a nozzle within the tunnel due to the substantial boundary layer growth. This will create higher flow velocities in the effective area in the tunnel outside the

boundary layer at 9 diameters of development than that occurring further upstream, continually evolving the flow conditions within the tunnel.

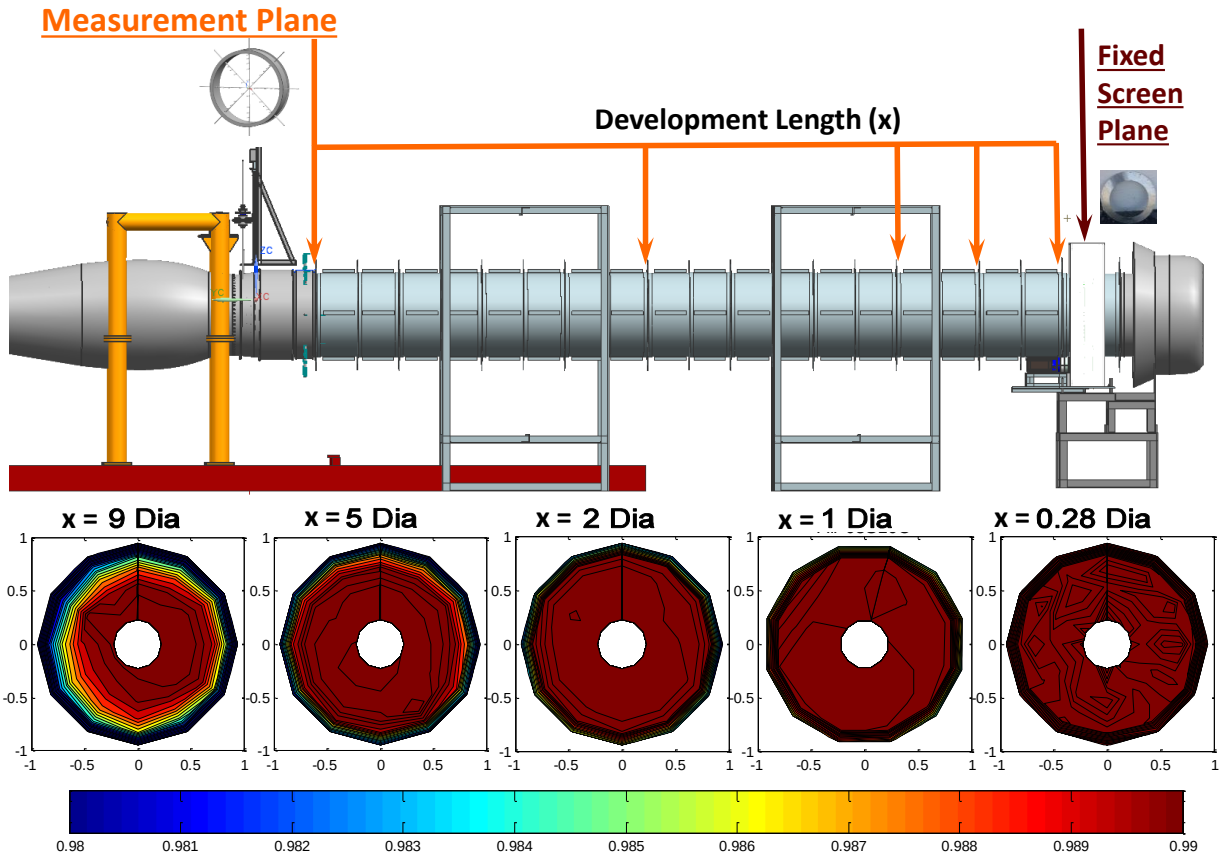

Figure 23. TPRA contour plots of undistorted tests performed in the long tunnel configuration (color axis in recovery).

The radial and circumferential measurements follow the orientation given in Figure 25-left. Figure 25-right further illustrates the flow uniformity within the tunnel. Each circumferential arm of the TPRA is plotted together for a sample test configuration. Similar results were obtained for all testing configurations considered. Since the results overlay with deviation within the measurement uncertainty, it was concluded that the tunnel flow was sufficiently uniform and that the tunnel could be used for further experimentation with the distorted cases.

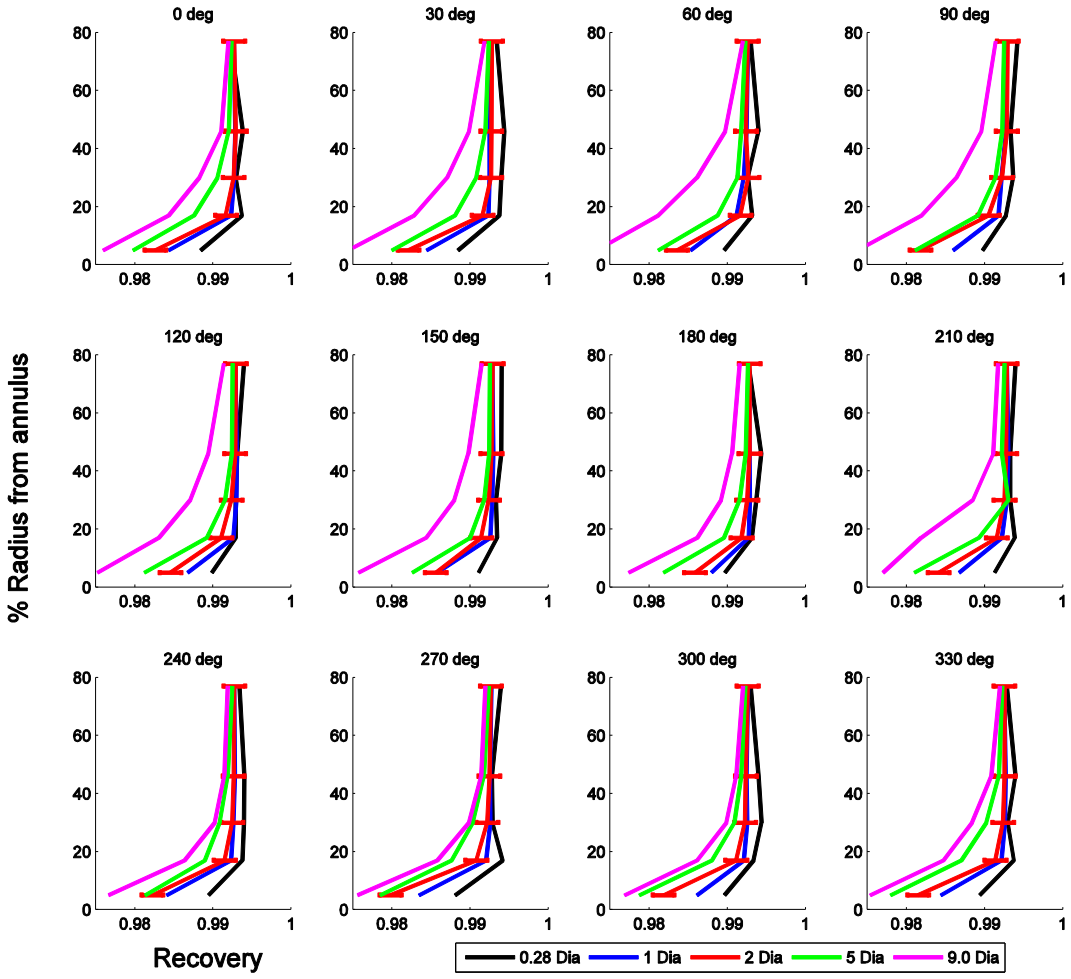

Figure 24. Boundary layer development of undistorted inlet profile through the tunnel.

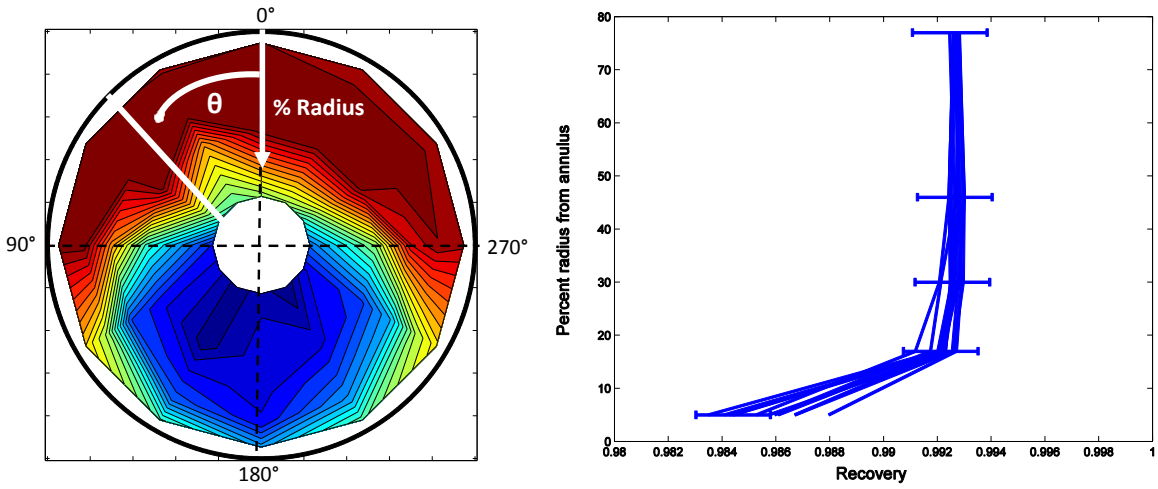

Figure 25. Radial and circumferential orientation for displaying TPRA data (left) and undistorted radial data for a sample test configuration (right).

Part I – Distortion Profile Development in the Duct

In the following sections, results are shown from a series of tests with the distortion screen installed 9.65 duct diameters upstream of the fan and the TPRA located at several locations downstream of the screen, starting at 0.28 duct diameters and ending at 9 duct diameters. This 'Long' tunnel configuration placed the screen sufficiently far upstream of the fan to prevent any interaction with the distortion screen and the fan face.

The color axis for all contour plots represents "Recovery" with respect to the reference atmospheric total pressure (Equation 9).

Time-Averaged TPRA Contours

The measured time-averaged recovery of the distortion profile is shown in Figure 26, represented as contour plots for increasing development length. Figure 26 is similar in structure to Figure 23 explained earlier. As shown, the distortion profile changes as it travels downstream of the screen. The high recovery region (shown as dark-red) is redistributed across the annulus in both a circumferential and radial migration to merge with the low recovery region (shown in dark blue at BDC). This distortion profile attenuation is a result of the mixing occurring between the low and high recovery regions. Comparing the 0.28 and 9 duct diameter development lengths, we see the difference in the circumferential recovery gradients. The 0.28 duct diameter development length shows a very large gradient between the high and low recovery regions. The 9 duct diameter development length, however, has a much smaller gradient between regions. The flow has had sufficient time to mix downstream of the screen, creating a smoother transition between the high and low recovery regions. The contours in between these two extremes show the intermediate stages of this development.

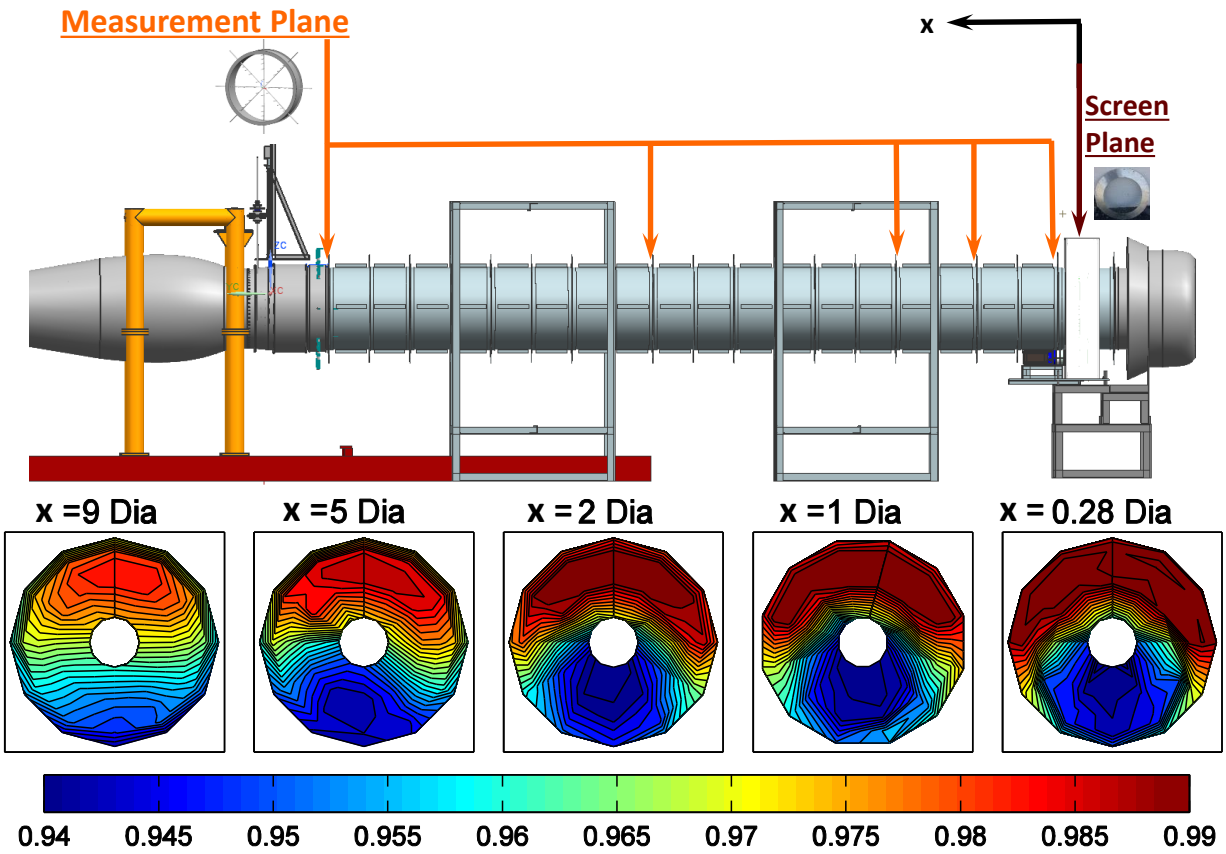

Figure 26. Distortion profile development with screen fixed at 9.65 diameters upstream of fan.

Part II – Fan/Screen Interaction

The second part of this study features a unique analysis into the interdependent relationship between the fan and screen. In the following paragraphs, results are shown for several tests completed where the development length established between the screen plane and measurement plane in Part I (0.28, 1, 2, and 5 duct diameters) was duplicated for 'Short' tunnel tests. These 'Short' tunnel tests placed the screen in closer proximity to the fan, where there exists an interaction between the fan and screen and the resulting distortion profile development is altered. These four 'Short' tunnel tests are compared with the 'Long' tunnel tests completed in Part I for equivalent development lengths to investigate the influence of fan proximity on distortion profile development.

Increased Development Length Time-Averaged TPRA Contours

Shown in Figure 27 is a collection of plots detailing the resulting total pressure profile 0.66 duct diameters in front of the fan face while the screen is moved closer to the fan face. The contour plots are viewed from left to right for decreased development length. As was mentioned for Part I, measuring the screen profile 9 duct diameters downstream of the screen plane results in a highly altered and attenuated total pressure distortion. Moving the screen plane closer to the fan face has the consequence of altering the resulting screen profile twofold; 1) the development length is shortened, decreasing the amount of mixing that can occur in the profile, and 2) the interaction between the screen and the fan is intensified and the fan begins to alter the development of the profile toward what was observed in Part I. Figure 27 shows that for

a fixed measurement plane in front of the fan, moving the screen closer to the fan face results in a more intense distortion profile, with higher circumferential gradients between high and low recovery regions. To detail the effect of fan presence on the development of the distortion profile, equivalent development lengths were studied by comparing the results obtained between Part I ('Long' tunnel) and Part II ('Short' tunnel). This is discussed in the following section.

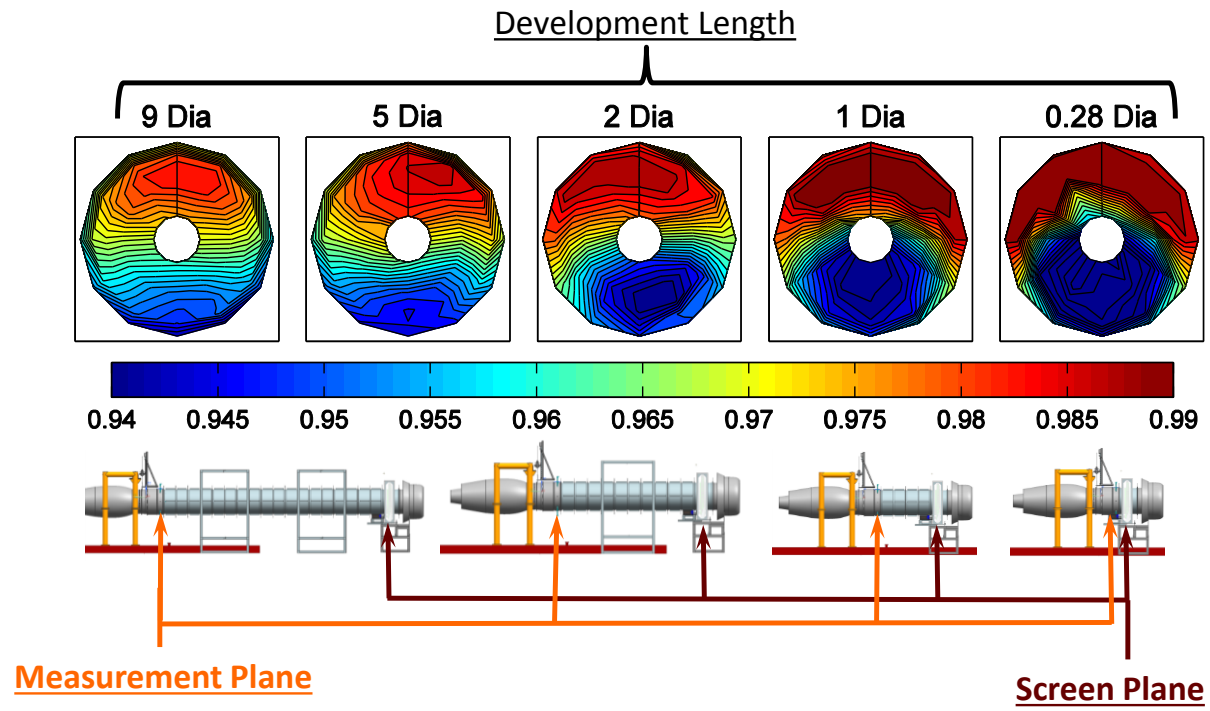

Figure 27. Contour plots of distortion profile for shortened development lengths and fan/screen spacing.

Comparative Development Length Time-Averaged TPRA Contours

Figure 28 is collection of contour plots from both Part I and Part II showing the distortion profile at equivalent development distances downstream of the screen, but with the screen at varying locations with respect to the fan. These profiles show the effect of screen-fan proximity on the development of the distortion profile. For example, in the far left column, both measured profiles correspond to 0.28 diameters of development, as indicated by their respective titles. The location of the TPRA with respect to the screen remains constant, but the screen position relative to the fan is altered. The experimental setup is shown above the top row profiles for the short tunnel configurations (close fan/screen positioning from Part II). An arrow indicating the respective location of the measurement plane in the long tunnel configuration (Part I) is shown in the bottom row of contours (long tunnel fan/screen positioning).

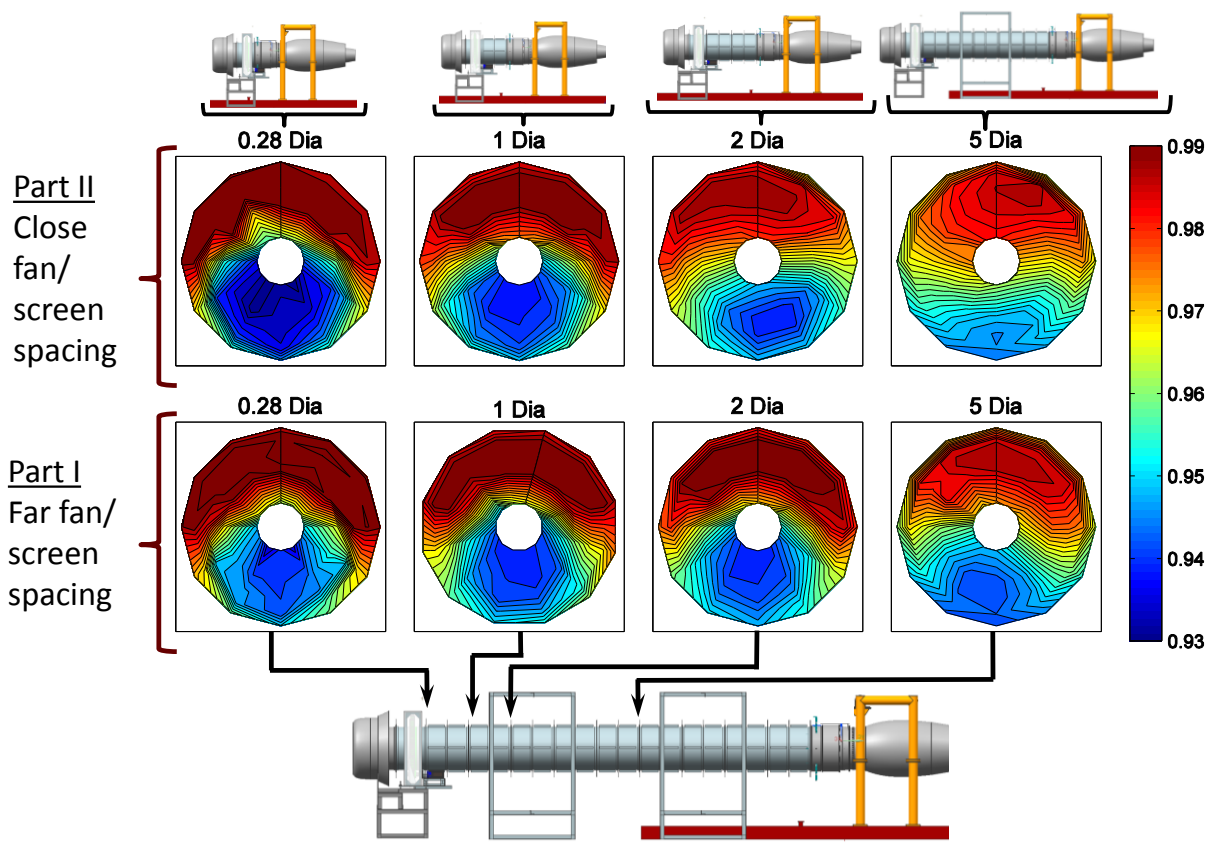

Figure 28. Contour plots of distortion profiles for varying development lengths and tunnel configurations. Top row represents 'Short' tunnel (Part II) and bottom row represents 'Long' tunnel (Part I).

As shown for 0.28 duct diameter development length (far left column), the resulting distortion profile is slightly different between the two configurations. For the short tunnel configuration (top-left), there is a stronger circumferential gradient into and out of the low recovery region at $\theta = 120°$ and $\theta = 240°$. This is indicative of the fan influencing (hindering) the development of the distortion. The increased static pressure in the tunnel in close proximity to the fan prevents the profile from developing properly, which is shown in the long tunnel configuration (bottom-left). High and low recovery circumferential extents appear to be preserved for both configurations.

A different behavior occurs for the increased development lengths. The 1 duct diameter development length shows no visually significant differences regarding the profile development. The 2 and 5 duct diameter development lengths show a reduction in the distortion intensity (increased recovery in the deficit region) as a result of the fan presence. Contrary to what was observed for the 0.28 duct diameter development length where the fan appeared to hinder the development of the profile, the 2 and 5 duct diameter development lengths show an increased mixing of the high and low recovery regions. This indicates that, at these locations, the fan is accelerating the mixing rate, reducing the circumferential and radial gradients of the profile between regions of constant recovery. The conclusions drawn from this behavior is that for these screen/fan positions, the screen is placed sufficiently far upstream of the fan face to be outside the static pressure gradient within the tunnel due to the blockage imposed by the fan, but close enough to have the development influenced by the fan rotation. For both development lengths, the extent and intensity of both the low and high recovery regions are altered, resulting in a less-intense distortion reaching the measurement plane. A quantified presentation of the results is presented in Chapter 5.

Chapter 5 - Discussion of Results

Summarized here is a detailed analysis of the results reported in Chapter 4. The data will be analyzed on a radial and circumferential basis to provide more information on the flow development and fan/screen interaction. Also included are ARP1420 distortion indices calculations and an investigation into the radial and circumferential gradients for varying development lengths. A detailed instrument uncertainty analysis is included in the Appendix. Statistical uncertainty was not evaluated for the data set due to the absence of repeated experiments. It is recommended by the author that future experiments should be repeated as required to reduce the statistical uncertainty by at least one-half the instrument uncertainty.

Part I – Distortion Profile Development

Introduced in Part I of Chapter 5 were contour plots showing the development of the distortion profile as it progressed in the constant diameter tunnel. Presented in the following sections is a more detailed analysis, looking at specific trends in the measured profile that were not captured in full-annulus contour plots. Included are time-averaged results on a radial and circumferential basis, a series of ARP1420 calculations that highlight the evolution of the profile, and radial and circumferential gradients for varying development lengths.

Radial TPRA Observations

If the recovery for each radius at given circumferential locations around the TPRA is plotted, a significant amount of detail can be observed with respect to the flow behavior. This was performed for four development lengths, as shown in Figure 29. Each subplot represents a collection of radial data sets for the four development lengths downstream of the screen at a given circumferential location, as indicated by the title. The ordinate of each subplot represents the distance from the annulus wall in percent-radius, increasing from the bottom of the plot at ‘0’ (tunnel outer-wall) to the top at ‘100’ (tunnel center). The abscissa corresponds to pressure recovery, increasing from left to right. Each radial measurement plot encompasses the four development lengths varying from 0.28 to 9 duct diameters.

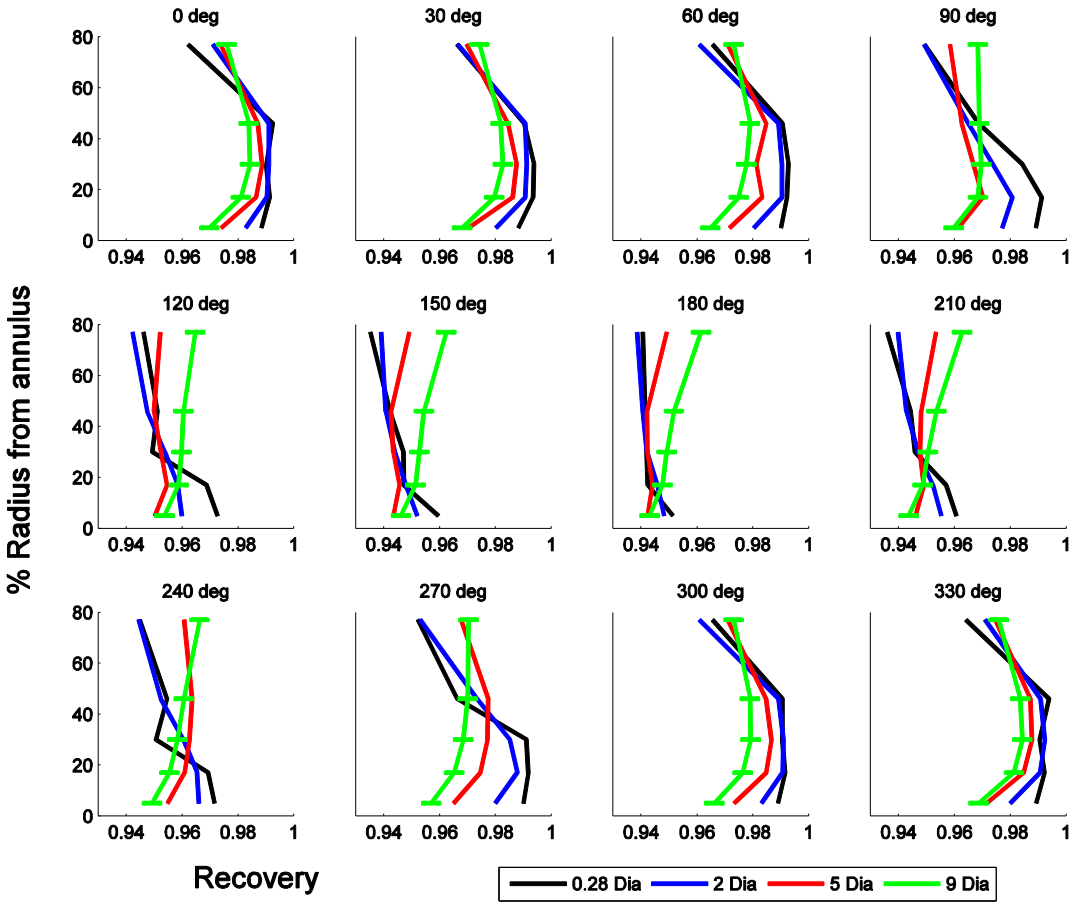

Figure 29. Plot of radial TPRA data for increasing development length at 12 circumferential positions.

Two important results of note are (1) the uniform decrease in recovery with increasing development length for radii less than 20% and (2) the increase in recovery for radii greater than 60% for all circumferential locations. The decrease in recovery for radii less than 20% can be accounted for through a simplified shear layer analysis.

As the development length is increased, the boundary layer thickens, lowering the shear stress and velocity gradient at the wall. The lower face-average recovery in the profile is a result of the turbulent conditions in the flow, where a high-speed aggressive mixing between the boundary layer and the free stream occurs, pulling more energy from the free stream and injecting it into the boundary layer. This process becomes more pronounced as the development length increases.

For radii > 60%, a similar mixing process occurs between the low recovery region ($120° \leq \theta \leq 240°$) and the high recovery region ($300° \leq \theta \leq 60°$). The high recovery region merges with the low recovery region, pushing the low recovery fluid circumferentially around the annulus, creating a swirling process that results in a higher recovery for radii greater than 70% at 9 duct diameters than at 0.28 duct diameters of development.

This mixing between the low and high recovery regions is most prevalent at the 180° circumferential location where the profile is initially exclusively in the low recovery region. As the flow develops, the mixing process extends nearly to the wall, where the high recovery flow has migrated and filled in the low recovery region up to and extending into the boundary layer. The high recovery region in the profile from

300° ≤ θ ≤ 60° shows a decrease in recovery for increased development length for radii < 20% due to boundary layer formation and for 20% < radii < 50% due to flow redistribution, It shows an increase for radii > 50%, where there exists a transition to the low recovery region. The difference in recovery for radii > 50% between the 9 and 0.28 duct diameter development lengths becomes more pronounced nearer to the low recovery region. In this low recovery region, 120° < θ < 210°, the local recovery increases for increasing development length as the high recovery flow is redistributed into the low recovery region.

A closer look at the radial measurements made at the 0, 90, and 180° circumferential locations (specified in the subplot titles) show the difference in boundary layer development for different regions in the profile. These measurements represent the high recovery, transitional, and low recovery regions and are shown in Figure 30. For the 0° case at the very top of the profile in the high-recovery region, we can see the influence of friction on the fluid at the wall (radii < 20%), thickening the boundary layer and lowering the perpendicular velocity gradient leading to lower recovery values for increasing development length. This recovery decrease for increasing development length is followed out from the wall until 65% radius where an increase in recovery is seen for increased development lengths for increasing radius. This is due to the high recovery region diffusing into the lower recovery region around the annulus, giving the impression that these locations are 'gaining' energy at the expense of the high recovery region. This recovery exchange location decreases in radius moving from the high recovery region (60% radius for 0°), into the transitional region (40% radius at 90°), and finally the low recovery region (15% at 180°).

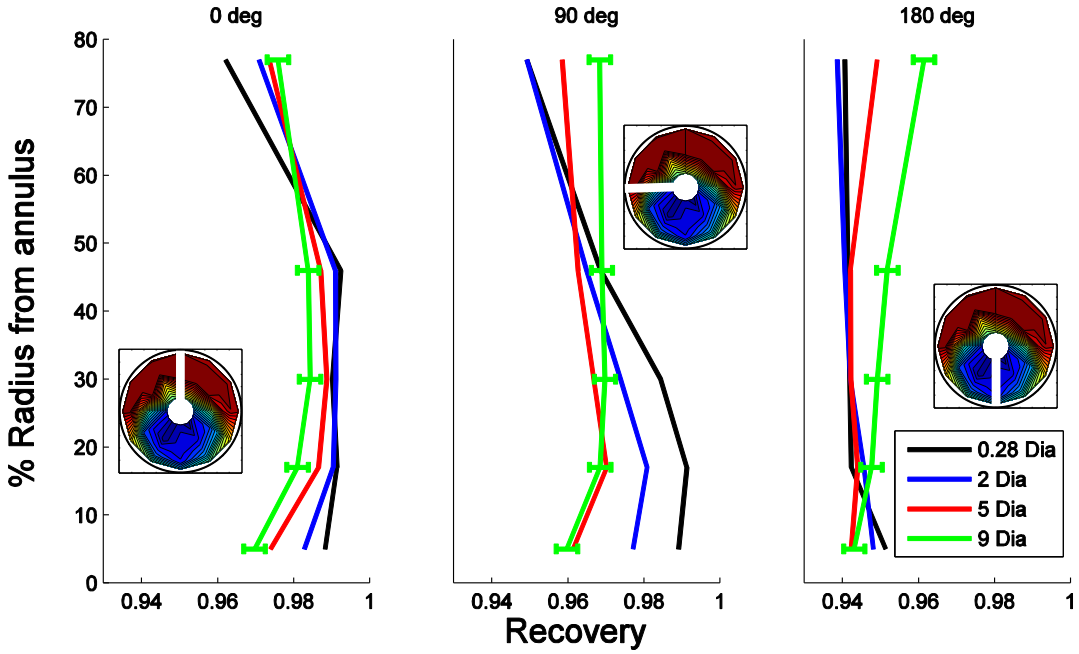

Figure 30. Radial TPRA measurements at 0° (left), 90° (center), and 180° (right) for increasing development length.

Less intensive boundary layer development is evident for the 180° radial measurements when compared to the 0° case. This is due to the redistribution of the high recovery flow being forced into the low recovery region, and as a result hindering the development of the boundary layer.

A final point regarding the radial flow development is the substantial boundary layer that results after 9 duct diameters of development. As was estimated in Figure 21-right, the boundary layer contributes to 22% of the tunnel diameter, effectively developing a nozzle within the tunnel. The increasing boundary layer height also increases the flow velocity outside of the boundary layer as the flow is forced through a smaller

effective cross section while maintaining a constant mass flow rate. The increased flow velocity helps accelerate the turbulent mixing occurring outside of the boundary layer.

Circumferential TPRA Observations

Another useful analysis of the TPRA data set is an investigation into the circumferential measurements made at the measurement plane. These 'rings' provide a circumferential set of measurements at five radial locations. Shown in Figure 31 are the circumferential measurements plotted for development lengths increasing from 0.28 to 9 duct diameters. The abscissa of each subplot is circumferential angle given in degrees, and the ordinate is given in recovery. Varying development lengths are shown and follow the legend given at the bottom of the figure. The radial and circumferential orientation follow the contour illustration in the bottom-right. All radii show a similar recovery magnitude for the low recovery region at 180°. Of particular note is the behavior of the mixing process as the radii is increased. The 5% radius plot shows a typical boundary layer-type development; increased development length reduces the circumferential recovery due to friction at the tunnel wall. As the development length increases, the boundary layer grows and higher momentum flow at the boundary layer's edge migrates further from the wall, lowering the momentum distribution in regions near the wall and resulting in lower recovery. Moving out from the wall results in a recovery increase in the low recovery region for increasing development length, and decreased recovery for the other regions. As shown in Figure 31, the increasing recovery in the deficit region increases in extent for increasing radius from the tunnel wall. This effect is not present at 5% radius, but beginning at 17% radius occurs for $140° \leq \theta \leq °220$ and increases in extent until it encompasses the entire annulus. This is due to the momentum transfer from the high recovery region to the low recovery region. Also evident is the accompanying increase in recovery in the deficit region for smaller development lengths for increasing radius from the tunnel wall. Although not prevalent until 77% radius from the wall, shorter development lengths show increased recovery for all circumferential locations. Momentum exchange is most uniform at the 77% radius case for 9 duct diameters of development.

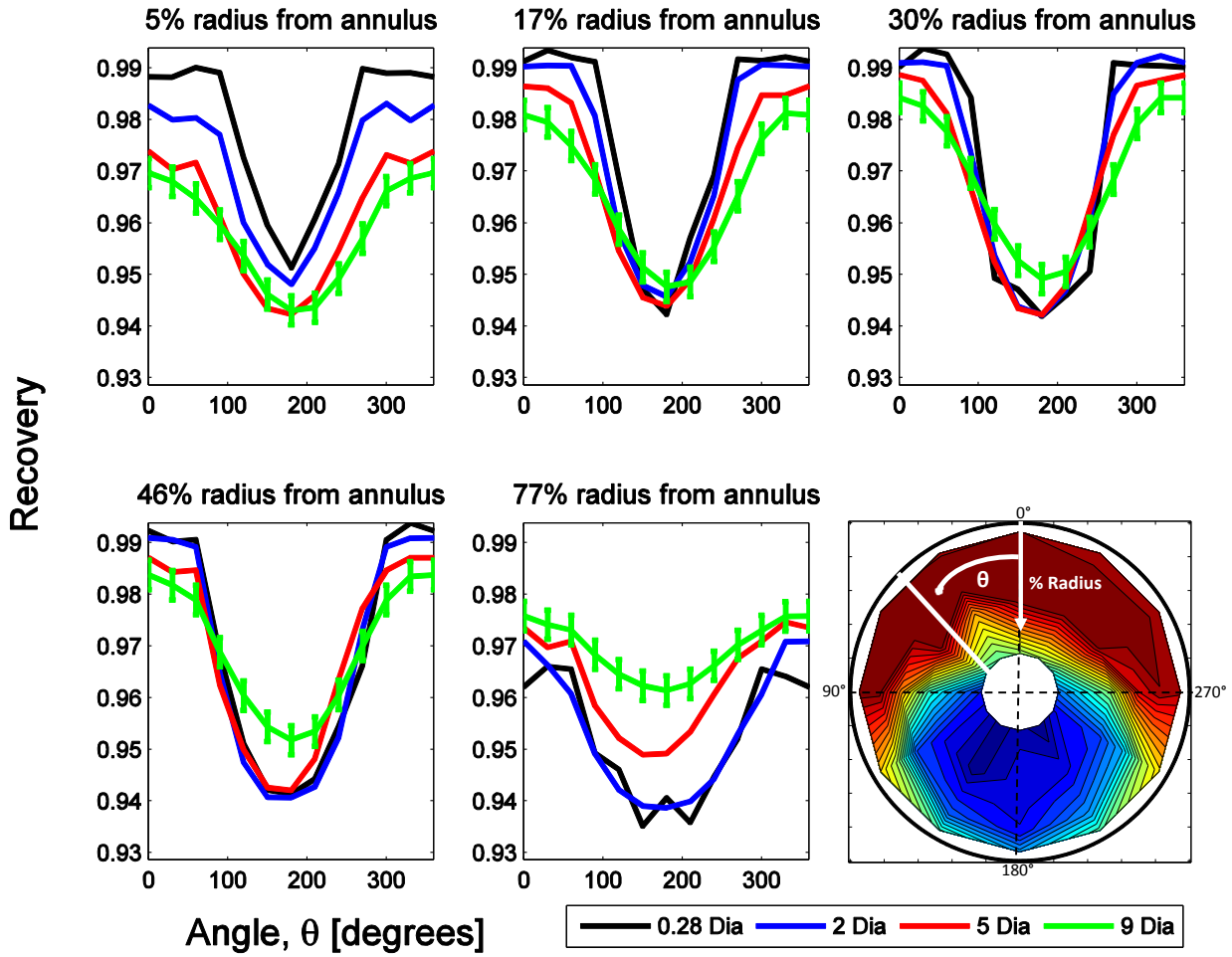

Figure 31. Circumferential TPRA measurements for increasing development length at 5 radius locations.

If the 0.28 and 9 duct diameter development lengths are looked at individually, the change in profile development can be more closely observed. Shown on the left of Figure 32 is a collection of all of the circumferential data for each radial location in the TPRA for a development length of 0.28 duct diameters. Shown on the right of Figure 32 is a similar plot, but for a development length of 9 duct diameters. For the development length of 0.28 duct diameters, increased radii results in a lower recovery value, especially in the deficit region at 180°. For the development length of 9 diameters, this process is reversed, with higher recovery values given for increased radii, a result of the flow exchange between the high and low recovery regions. Comparing the two plots in Figure 32, the low recovery distortion still persists after 9 duct diameters of development, albeit in an attenuated form. The overall recovery of the distortion profile is lower at the 9 diameter position due to the higher losses accumulated from friction and mixing, and the distortion intensity is much lower (higher recovery in deficit region), at the cost of a wider distortion extent. Additional comments on the variation of the distortion profiles is given in the following sections.

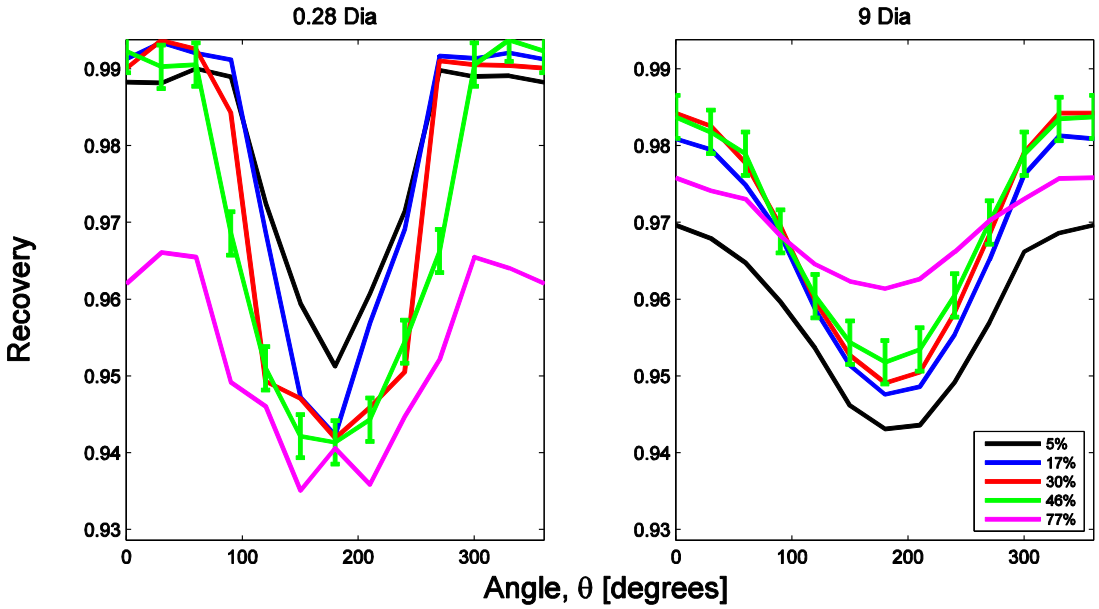

Figure 32. Circumferential TPRA measurements for 0.28 and 9 diameter development lengths at five radial locations.

ARP1420 Statistical Analysis

Following the results presented in the previous section, an ARP1420 analysis provides further insights into the downstream mixing occurring in the profile and allows a discussion utilizing more common distortion descriptors to characterize the profile. Figure 33 summaries these results with regards to circumferential distortion intensity, circumferential extent, and radial intensity, which were defined in Chapter 3. The legend for all plots is given in the bottom subplot of Figure 33 in percent radius from the inner tunnel wall (5-77%). The top plot of Figure 33 shows the attenuation of the circumferential distortion intensity as the profile develops in the tunnel for each measurement radii, a consequence of the cumulative mixing and frictional losses as it traverses the duct. Intensity is strongest for the 30% radius case due to the expansive high recovery region, short transition region, and intense low recovery region at 180°. Also, because this radii is in between the tunnel-wall and tunnel-center locations, it is less affected by the frictional losses at the wall and turbulent mixing in the center of the annulus. The 77% radius has the lowest distortion intensity since the high recovery region does not extend that far out from the wall lowering the circumferential gradients between recovery regions.

The circumferential distortion extent (Figure 33-center) can vary as much as 20-25° for increased development lengths, with most of the changes occurring at 5% radius. Increasing development length allows more effective mixing between recovery regions so that a near-uniform extent is reached after 5 duct diameters. Extent increases after 5 duct diameters as the magnitude of the average pressure drops more rapidly than the average pressure in the deficit region. At 5% radius, extent increases as the low recovery region is diffused circumferentially around the annulus, creating a more expansive deficit region with respect to the average ring pressure.

Boundary layer development in the low recovery region is not as aggressive as in the high recovery region as more fluid from the high recovery region has redistributed itself into the low recovery region, discouraging effective boundary layer formation and growth. As a result, the high recovery region exhibits higher losses in the boundary layer for increased development length, lowering the relative difference

between the average circumferential pressure and the average pressure within the deficit, increasing the extent of the distorted region.

The bottom plot of Figure 33 shows the radial intensity for increasing development length. Changes in relative face-average pressure are most severe at 5% and 77% radius, with 5% radius initially at a negative radial intensity and then switching to a positive value for increased development length. Initially, the 5% radius location contains a high total pressure relative to the face average due to the circumferentially expansive high recovery region. The thickening boundary layer as a result of increased development length lowers the recovery at these radii until it is below the face average pressure at a development length of 5 duct diameters. Continued development lowers the circumferential average pressure with respect to the face average pressure. An opposite trend occurs at 77% radius where a large portion of the circumferential flow is in the low recovery region and does not extend into the high recovery region. As a result, the average circumferential pressure is below the face average pressure and contributes to a positive radial distortion intensity. As the turbulent mixing conditions at the center of the tunnel proceed downstream of the screen, the average circumferential pressure decreases in magnitude relative to the face average, until a near uniform value is obtained for all radii > 5%. At 5% radius, the radial intensity will progressively increase in magnitude until fully developed conditions are obtained.

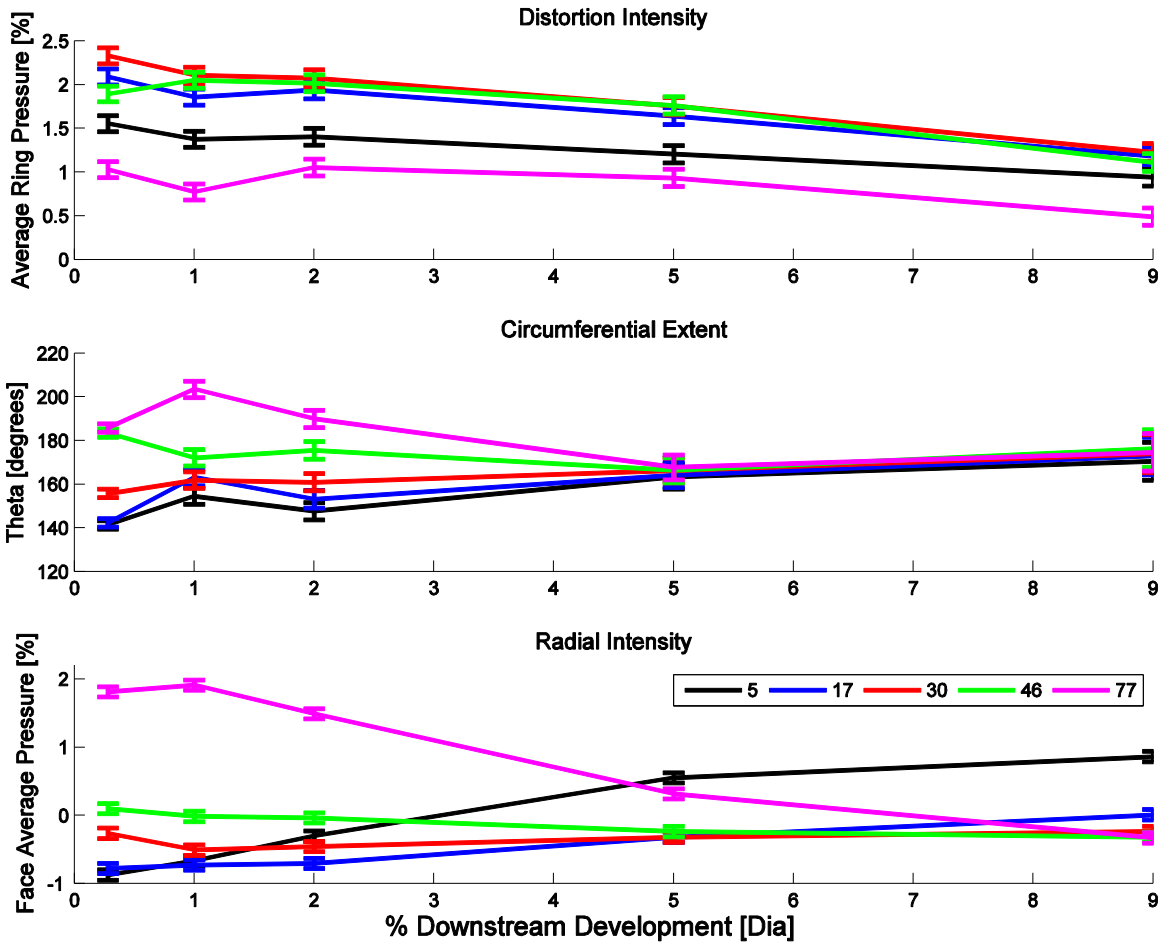

Figure 33. ARP1420 analysis for increasing development length at 5 radius locations.

Gradients

Another important aspect to consider regarding distortion profile development is the circumferential and radial gradients between the recovery regions. Moving circumferentially around the distortion profile (as a fan blade would), large local pressure changes can lead to operating instabilities. The magnitude and duration of the gradient is an important feature for distortion tolerant fan design. Shown in Figure 34 is a plot of the circumferential gradients between successive circumferential measurements for increasing development length. The attenuation of the distortion profile is evident by the decreasing magnitude of the gradients travelling into and out of the deficit region for increasing development length. Although the magnitude of the gradients vary from 5% to 77% radius, there is a change in the incoming distortion pattern across the entire surface area of the profile. This is indicative of a full blade span distortion, with a sharp change in the incoming flow velocity occurring twice for each blade rotation (into and out of the deficit region). Higher gradients occur for 17% < radii < 46% as these regions encompass both the high recovery and low recovery regions. Gradients do not vary to the same magnitude for radii > 5%, as the most intense distortion in the deficit region is located near 77% radius, however the 77% radius measurements do not extend into the high recovery region at 0°, lowering the gradient. Small gradients are focused at 0° and 180° as these correspond to circumferential midpoints of the high and low recovery regions, respectively, which contain a 60-180° extent depending on radius.

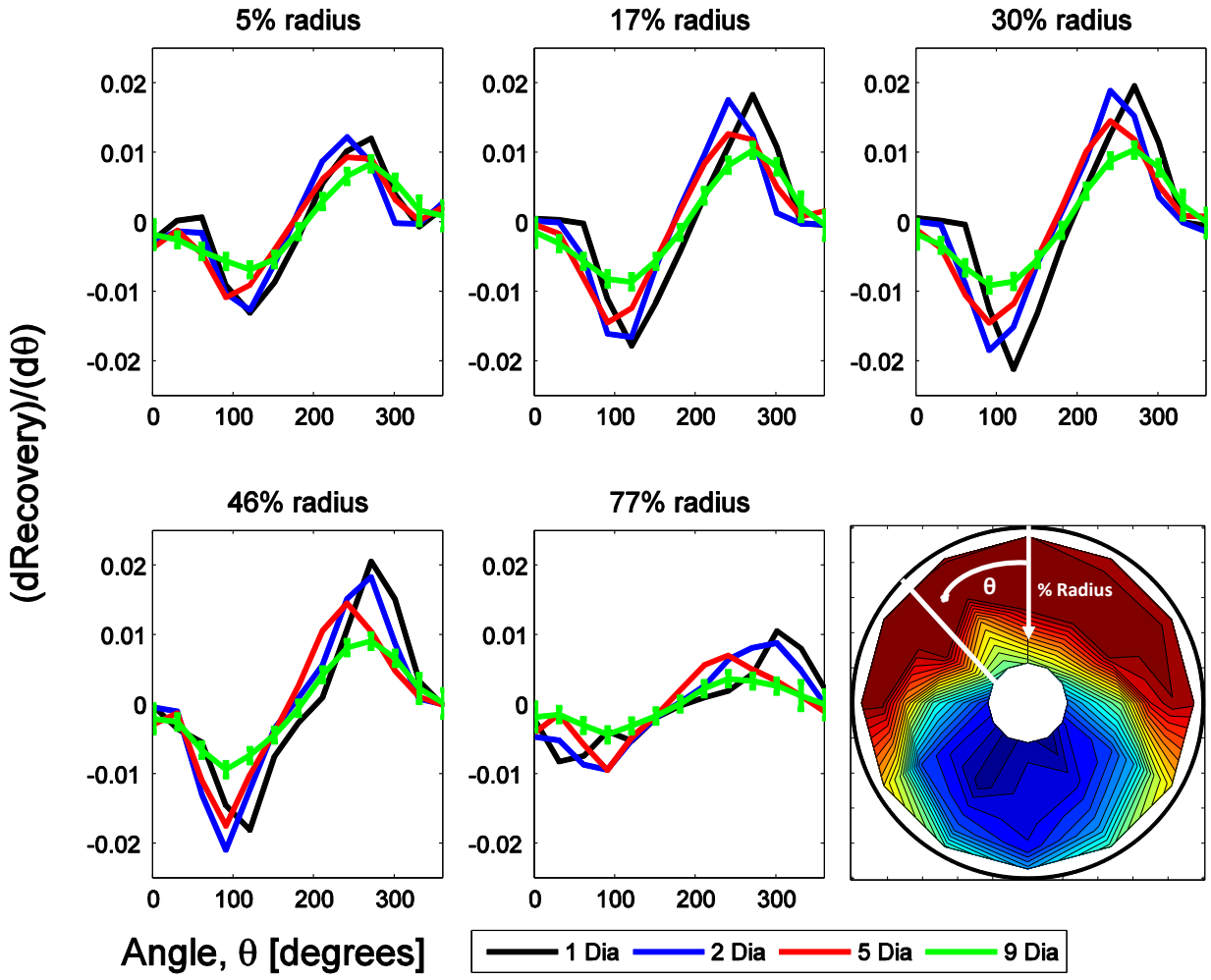

Figure 34. Plot of circumferential gradients for increasing development length at 5 radius locations.

Shown in Figure 35-left is a plot of the maximum circumferential gradient for increasing development length at each radial location. The maximum gradient between circumferential locations decreases for increasing development length, with slightly inconsistent behavior at 46% and 77% radius. The 5% and 77% radius locations exhibit lower circumferential gradients due to the more effective mixing occurring in those regions, either from the high and low recovery regions mixing together (77% radius) or from the entrainment of higher momentum fluid in the boundary layer (5% radius). These radii also do not include both the high and low recovery regions for the entire circumference, limiting either the maximum (77%) or minimum (5%) values the circumferential values encompass, lower the maximum gradients. The 5% radius case passes through an extensive high recovery region near the top of the profile, but the deficit region it includes is not as low in recovery as for radii > 5%. Alternatively, the 77% radius encompasses an intense distortion at 180°, but does do include the higher recovery values that is included for radii < 77% for 300° ≤ θ ≤ 60°. The 17% and 30% radius measurements are between these locations, encompass both the expansive high recovery region and an intense low recovery in the deficit region, and do not have as effective mixing as for the 5% and 77% radius, thus higher gradients. It is important to note that although there is an attenuation of the distortion intensity, gradients, and thus varying recovery regions, are still present after 9 duct diameters of development.

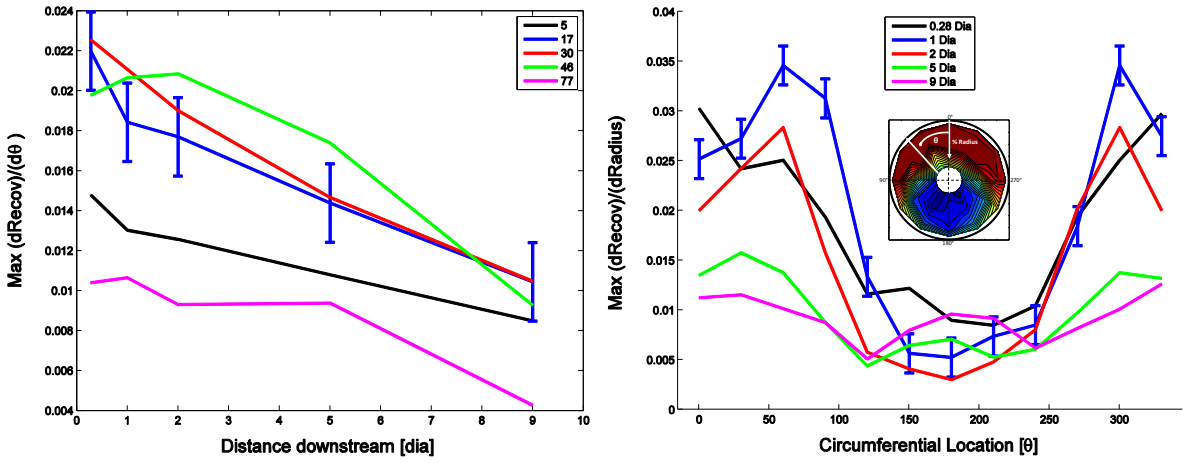

Figure 35. Maximum circumferential (left) and radial (right) gradients for increasing development length at 5 radius locations (left) and varying circumferential location at 5 development lengths (right).

Shown in Figure 35-right is a distribution of the maximum radial gradients present in the distortion profile for increasing development length. The largest gradients are focused at 60° and 300° where the transition between the high and low recovery regions exists. This location experiences rapid magnitude drops for the first 5 duct diameters of development, but further development results in smaller radial variations. The low recovery deficit region at 180° shows an increase in the radial distortion gradient for the 5 and 9 duct diameter development lengths due high recovery flow redistributing itself into this region. The smallest radial gradients occur in the low recovery region, as it extends radially from 5% to 77% radius, while the high recovery region is not as radially expansive and encompasses some of the deficit region at 77%. Comparing Figure 35-left and Figure 35-right, the radial gradients are slightly higher in magnitude than the circumferential gradients, indicating higher radial mixing, even though the distortion is circumferentially-dominated.

Part II – Fan/Screen Interaction

The second part of this study investigated the interaction between the screen and fan. As stated in the literature review, this important interaction determines what profile ultimately enters the fan with the distortion screen moved closer to the fan. Determining this interaction is critical in analyzing fan performance subject to total pressure distortion when the screen is located at a fixed distance relative to the fan. By performing a series of analyses with the measurement plane located at 0.28, 1, 2, and 5 duct diameters downstream of the screen and the position of the screen relative to the fan face altered between ‘Short’ and ‘Long’ tunnel configurations, the effect of the fan on distortion profile development was investigated. As discussed in the experimental design of Chapter 3, it was assumed that the long tunnel configuration placed the screen sufficiently far upstream of the fan such that the screen produced profile was unaffected by the fan presence. By moving the screen profile closer to the fan face, the interaction between the screen and fan was investigated for equivalent development lengths.

Radial TPRA Observations

The first step in analyzing the differences in the developed profiles from the Part I and part II investigations is to determine where the greatest discrepancies between screen/fan positions occur. This can

be accomplished by observing the *differences* in measured recovery between the short and long tunnel configurations at equivalent locations in the TPRA. This is shown in Figure 36. Moving in a counter-clockwise manner about the TPRA (co-rotating with the fan), the largest differences between the long and short tunnel configurations occur for the 60°, 90°, 210°, and 240° circumferential locations, which corresponds to moving out of the high (60° and 90°) and low (210° and 240°) recovery regions: the exiting transitional regions. This is indicative of asymmetrical mixing occurring within the profile. For example, the 60° and 90° circumferential locations should exhibit equal differences between short and long tunnel configurations at 300° and 270° as well, since these are the mirrored positions on the other side of the profile; however, this is not the case. This is considered to be most likely a consequence of the turbulent conditions within the tunnel preventing predicted and well-behaving mixing between regions, and not due to screen construction and placement inaccuracies.

The radial difference plots of Figure 37, for an undistorted flow with the uniform backing screen placed in the measured positions, and show profiles that are essentially independent of fan position relative to the screen.. This verifies that the effects evidenced in the distorted screen cases are a function of the distortion screen, and not the backing grid or any unaccounted tunnel effects.

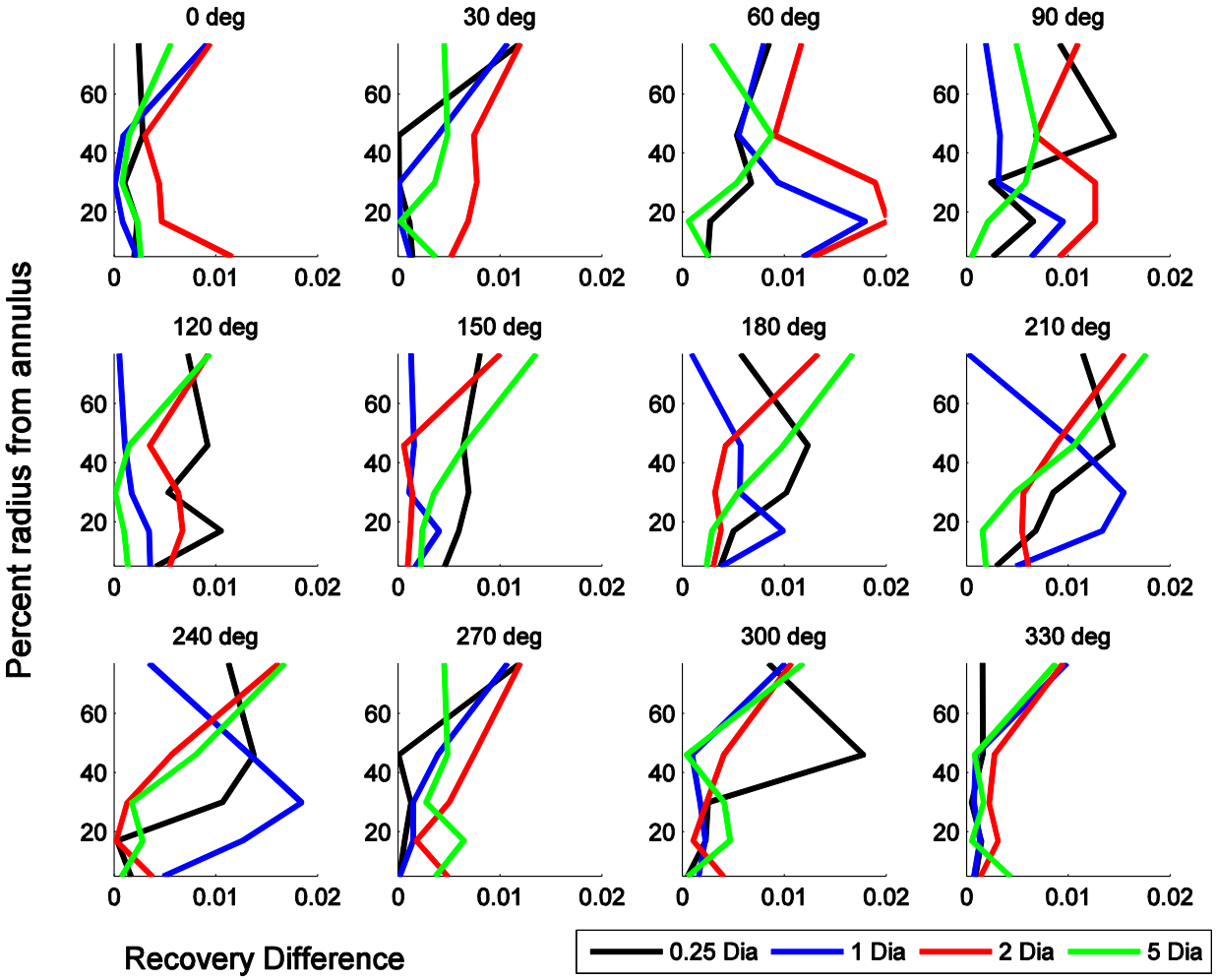

Figure 36. Distorted radial recovery *differences* for equivalent development lengths at 12 circumferential locations.

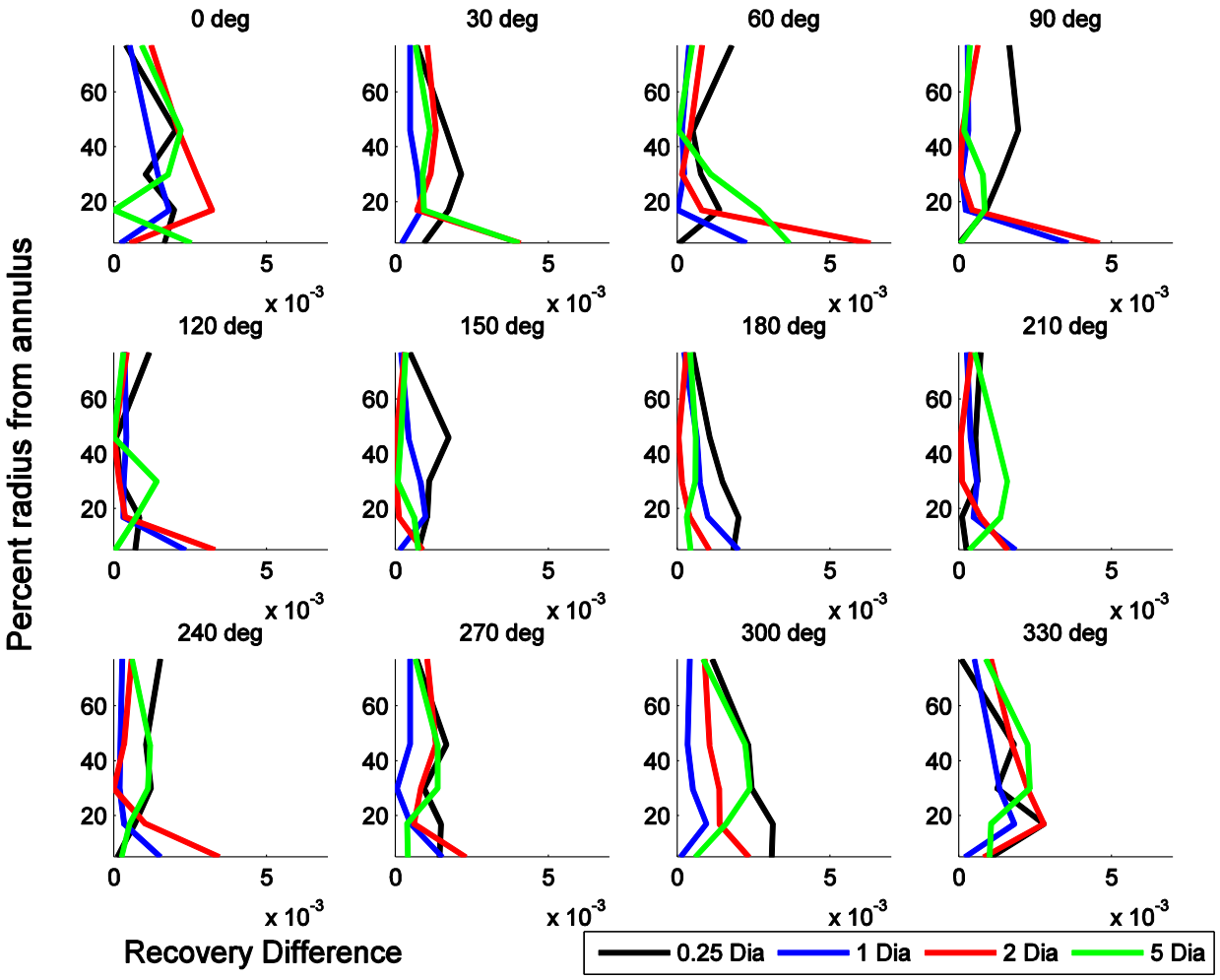

Figure 37. Undistorted radial recovery *differences* for equivalent development lengths at 12 circumferential locations.

The radial TPRA analysis is continued in Figure 38 for the 60°, 90°, 210°, and 240° circumferential locations that were found to be of interest in Figure 36. Percent radius from the tunnel wall is given on the ordinate, increasing from bottom (0%) to top (80%), and the values of the measured recovery rather than the differences for the Part I and Part II experiments, is given on the abscissa, increasing from left to right. For each development length (row) the largest discrepancy occurs at 77% radius; thus the fan is seen to have a larger effect on the mixing between the high and low recovery regions, as opposed to the boundary layer development. For all circumferential locations, the 5% radius measurements show close agreement. For the 210° circumferential location (moving out of the distortion), the discrepancy between the short and long tunnel configurations increases for increasing development length at 77% radius. The higher recovery values at 77% radius are evidence of the increased mixing of the distortion profile due to the fan presence (1-5 duct diameter development lengths). For small development lengths (0.28 duct diameters), the fan inhibits effective mixing of the pressure regions, resulting in a lower recovery region than for the 'Long' tunnel configurations outside the fan presence.

For very short development lengths and fan/screen spacings (≤ 0.28 duct diameters), the fan imposes a static pressure gradient in the tunnel due to its blockage of the duct. This inhibits natural development of the distortion profile and prevents effective mixing. From the results presented in Figure 37, a development length of 1 duct diameter appear to be the transition location where the screen and measurement plane are

placed sufficiently far upstream of the fan face to be outside this static pressure gradient influence. Profile development is still altered, however, by the rotational nature of the fan, which appears to increase the mixing rate of the recovery regions. This fan-enhanced mixing for the sort tunnel configuration is continued to the maximum measured distance of 5 duct diameters of development for 77% radius at 90° and 210°.

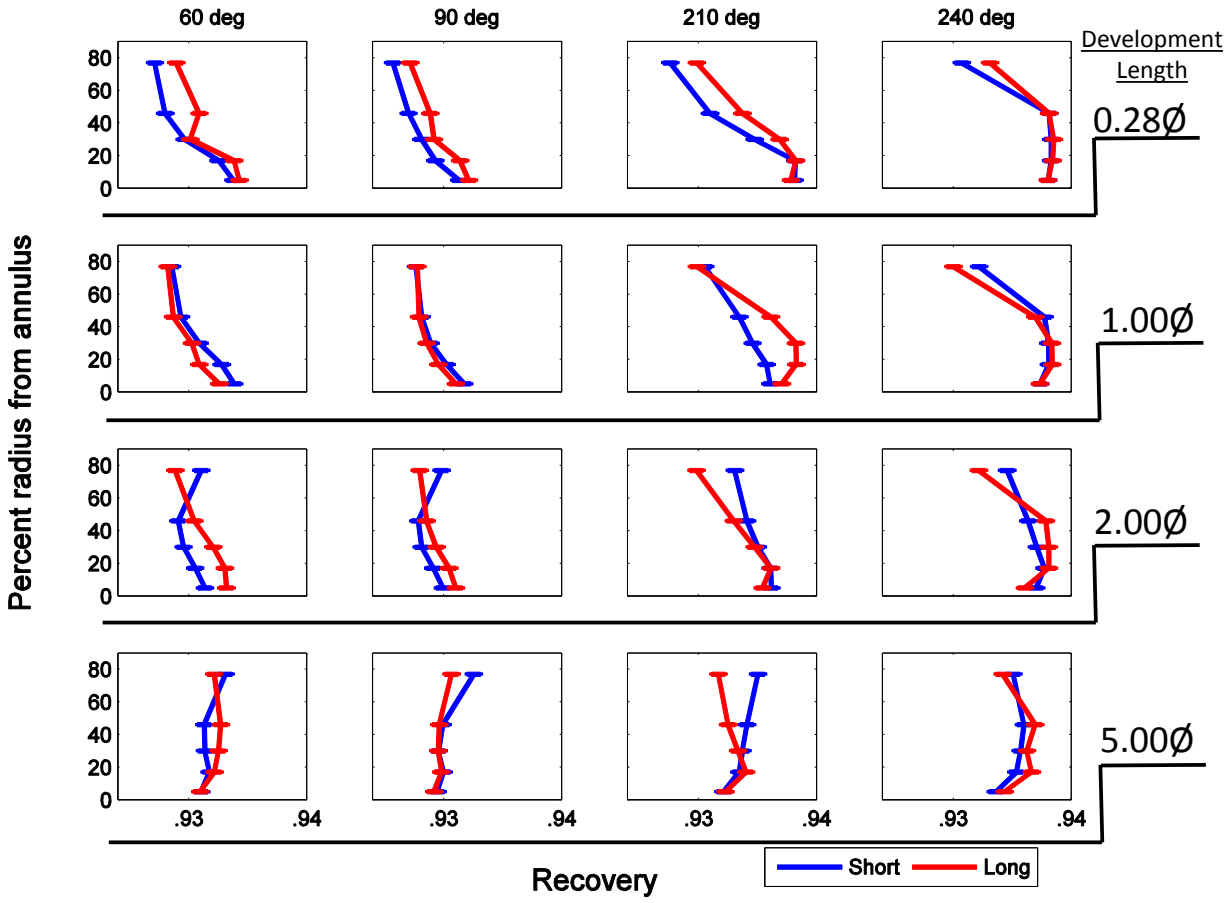

Figure 38. Recovery plots for distorted equal spacing cases in primary mixing locations located circumferentially around the TPRA (60, 90, 210, and 240°).

Circumferential TPRA Observations

As was shown in Part I, a circumferential analysis of the TPRA data for increasing development lengths highlights some of the interesting points regarding profile evolution. Figure 39 shows a circumferential plot of the TPRA data, where the rotation angle is measured from 0° at TDC in a counter-clockwise motion. Recovery is given on the ordinate and circumferential location is given on the abscissa in degrees. Development length varies by row and corresponds to the heading 'Development Length' given on the far right. For a development length of 0.28 duct diameters (1st row) there is little difference between the short and long tunnel configurations in the high recovery regions ($0° \leq \theta \leq 60°$ & $300° \leq \theta \leq 0°$). There is a much larger difference in the low recovery region, being the largest at 77% radius (5th column), where the short tunnel configuration exhibits a lower recovery. This is presumed to be an effect of the fan blockage causing a static pressure rise in the tunnel upstream of the fan and perturbing the flow development as was seen in the radial plots of Figure 38.

For increased development lengths (1, 2, and 5 duct diameters) the discrepancy between the short and long tunnel configurations for the high recovery region is indistinguishable. At 77% radius for a development length of 1 duct diameter (2nd row, 5th column), there exists a similarity between the short and long configurations at 180°. The transitional and higher recovery regions outside of the low recovery deficit region ($0° \leq \theta \leq 120°$ & $240° \leq \theta \leq 0°$) show higher sensitivity to screen placement relative to the fan. Higher recovery values indicate enhanced mixing, a result of the engine rotation. This indicates that the static pressure gradient mentioned earlier as preventing effective mixing for the short tunnel configuration at 1 duct diameter of development, does not hinder mixing circumferentially for regions outside of the low recovery deficit.

The 2 and 5 duct diameter development lengths show the short tunnel configuration exhibiting more circumferential mixing and migration of the high recovery region, which is most evident at 77% radius. In conclusion, for small development lengths (less than 1 duct diameter) the fan is close enough to the screen to hinder the natural development of the profile, but for increased development lengths (1-5 duct diameters), the presence of the fan accelerates the mixing process, resulting in a more attenuated profile than without the downstream fan presence. It is probable that the fan would continue to influence the distortion profile development for increased development lengths.

Figure 40 is a plot similar to Figure 39 but using the undistorted backing screen, showing the circumferential recovery differences between the two tunnel configurations is within the measurement uncertainty of the experiment for all radii and development lengths, and the effects observed in Figure 39 are a result of the distortion screen.

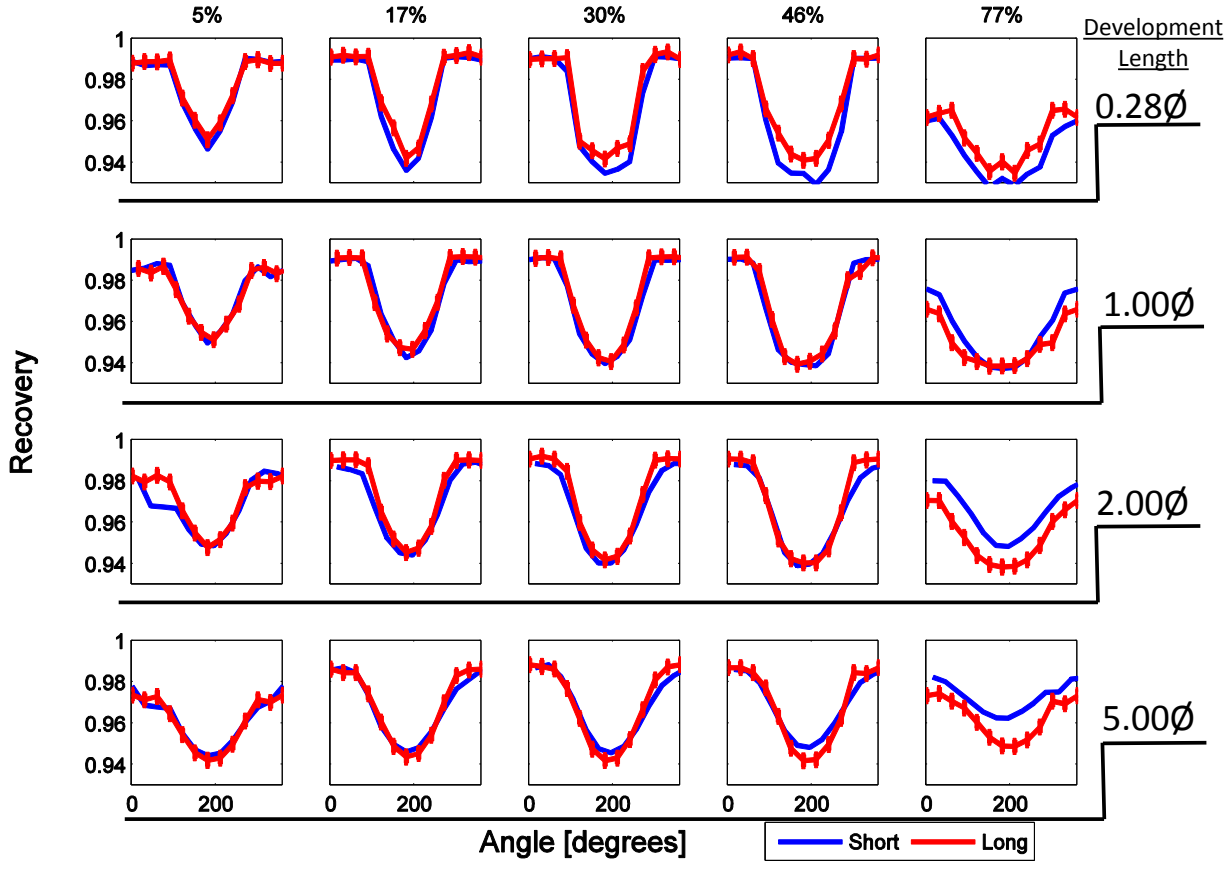

Figure 39. Circumferential distorted TPRA data for equivalent development lengths at five radial locations.

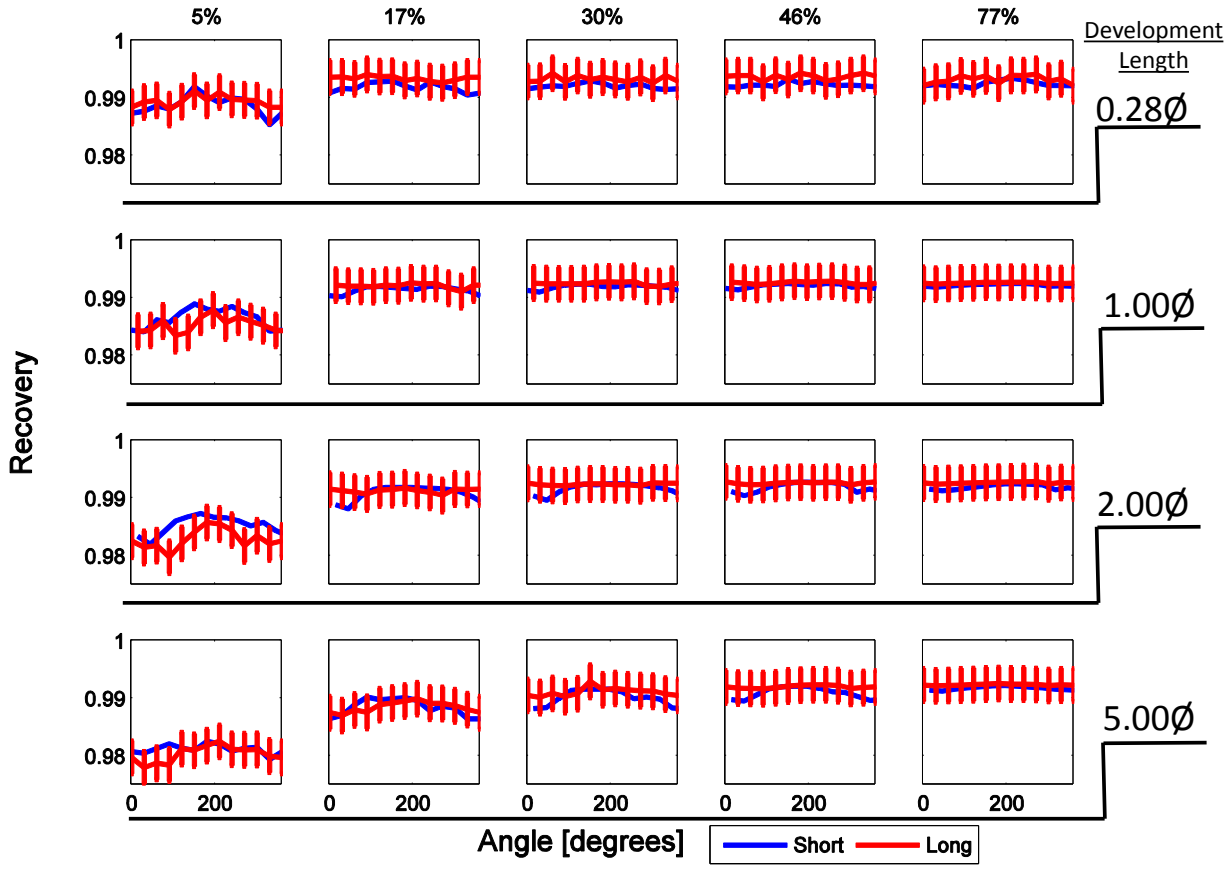

Figure 40. Circumferential undistorted TPRA data for equivalent development lengths at five radial locations.

ARP1420 Statistical Analysis

Figure 41 shows the results of an ARP1420 distortion indices analysis for the equivalent development lengths. Each column is a different distortion descriptor indicated by the respective titles on the first row. The ordinate of each subplot is equal for each column, corresponding to the descriptor. The abscissa of each subplot is given as percent radius from the inner annulus wall. Each row is a different development length as indicated on the far right of the figure under the heading 'Development Length'. The left column represents the circumferential distortion intensity of the profile, showing larger intensity for the short tunnel configuration at a development length of 0.28duct diameters (1st row) for radii < 77% due to the fan hindering effective mixing mentioned previously. For a development length of 1 duct diameter, close agreement is shown between the short and long tunnel configurations except at 77% radius where the higher recovery values seen at this radius and spacing in the high recovery region of Figure 40 attribute to the higher distortion intensity. Distortion intensity is lower for increased development lengths (2-5 duct diameters) in the short tunnel configuration, evidence of the enhanced mixing of the rotor explained in previous sections when the screen is placed far enough upstream to be outside the blockage effect.

The distortion extent (center column) is very similar for both tunnel configurations at a development length of 0.28 duct diameters, with a small discrepancy for radii > 60%, although within measurement uncertainty. The extent of the distortion begins to 'level out' across all radii for increased development length (1 to 5 duct diameters). The uniform circumferential extent is a result of mixing; the high recovery region redistributing the flow to give a uniform 'attenuated' distortion for all radii. Initially, radii < 5% have a relatively low circumferential extent, with the highest magnitude occurring at 77% radius. Due to the radial and circumferential flow redistribution, the extent becomes near-uniform after 5 duct diameters of development across all radii. The 'Long' tunnel configuration attenuation is not as rapid, as evidenced by the higher slope from 5-77% radius for 1 and 2 duct diameter development lengths. Once 5 duct diameters of profile development has occurred, however, the extent follows a near-uniform distribution similar to the 'Short' tunnel configuration, albeit at a lower magnitude. The 'Short' tunnel configuration exhibits a higher distortion extent at 5 duct diameters of development due to the improved mixing effect of the fan. Also, the intensity of the profile is lower at 5 duct diameter of development across all radii, lowering the face average total pressure. This lowers the relative difference between the low and high recovery regions, increasing the circumferential extent.

For the radial intensity (right column) there exists a large discrepancy between the short and long tunnel configurations at 77% radius for 1, 2, and 5 duct diameters of development. A larger radial intensity is present in the 'Long' tunnel configuration due to the fan presence in the 'Short' tunnel configuration which enhances the mixing between the high and low recovery regions, reducing the absolute and relative radial distortion at 77% radius. The radial intensity is initially more intense (lower negative value at 5% radius and higher positive value at 77% radius) for a development length of 0.28 duct diameters due to the rising static pressure gradient immediately upstream of the fan, hindering proper profile development, an effect seen in earlier analyses. After 5 duct diameters of development the intensity for the short tunnel configuration has dropped to a negative value, indicating the ring average pressure has moved below the face average in the distortion while the long tunnel configuration remains a positive value.

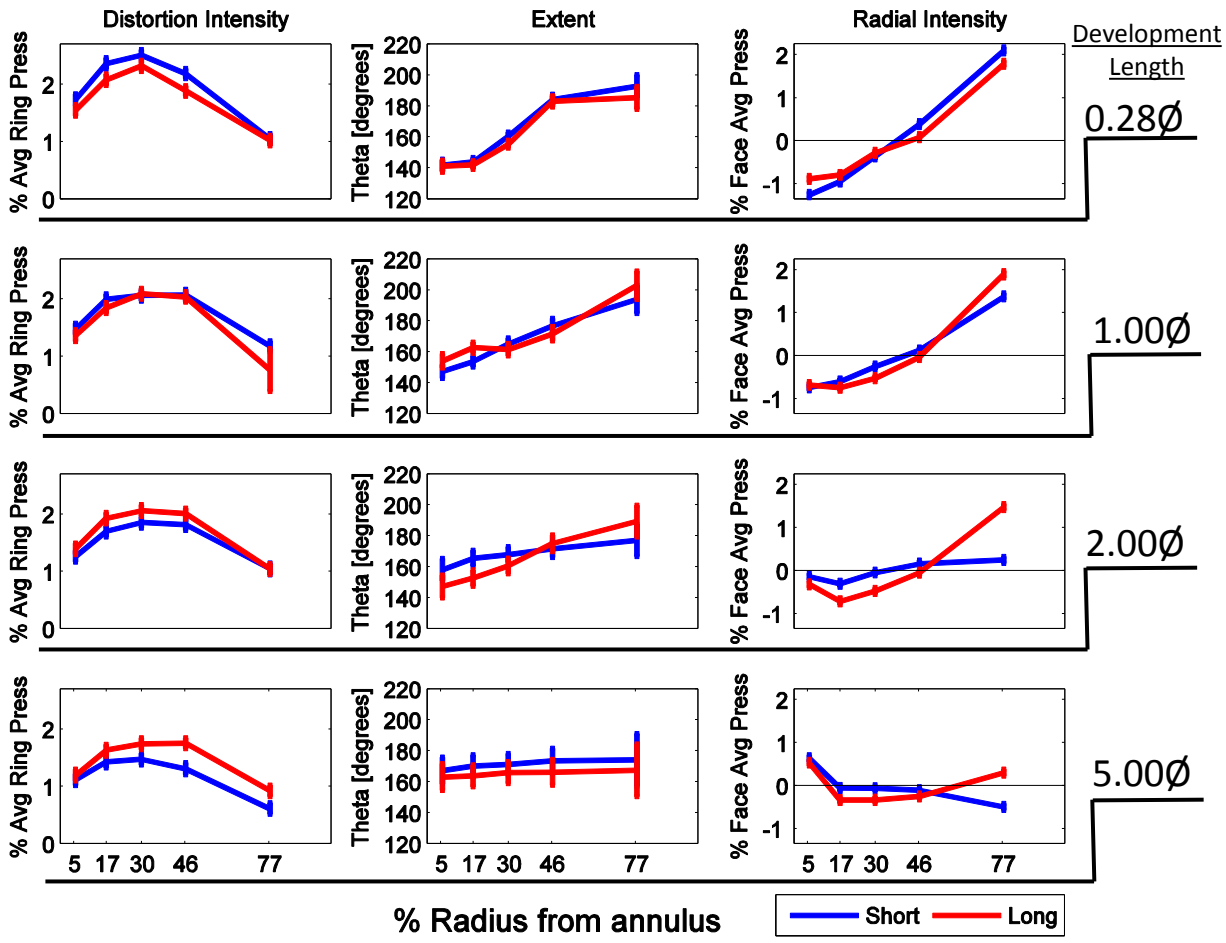

Figure 41. ARP1420 distortion indices for equivalent development lengths increasing radii.

Gradients

Shown in Figure 42 is a plot of the maximum circumferential profile gradients for equivalent development lengths. Each subplot represents a different development length, indicated by their respective titles. The ordinate is the recovery gradient for neighboring circumferential locations. The abscissa is percent radius from the inner annulus wall. The gradients are initially higher in the 'Short' tunnel configuration for the 0.28 duct diameter development length due to the static pressure gradient induced by the fan presence explained earlier. Larger gradients in the 'Long' tunnel configuration appear for increasing development lengths (1-5 duct diameters), a consequence of the fan proximity for the 'Short' tunnel configuration enhancing the mixing between low and high recovery regions. The largest discrepancy between tunnel configurations appears in the 0.28 duct diameter development length at 46% radius. Large differences also appear in the 5 duct diameter development length at 30% and 77% radius. For all development lengths and configurations, the largest gradients appear at the 46% radius location, an effect explained in Part I.

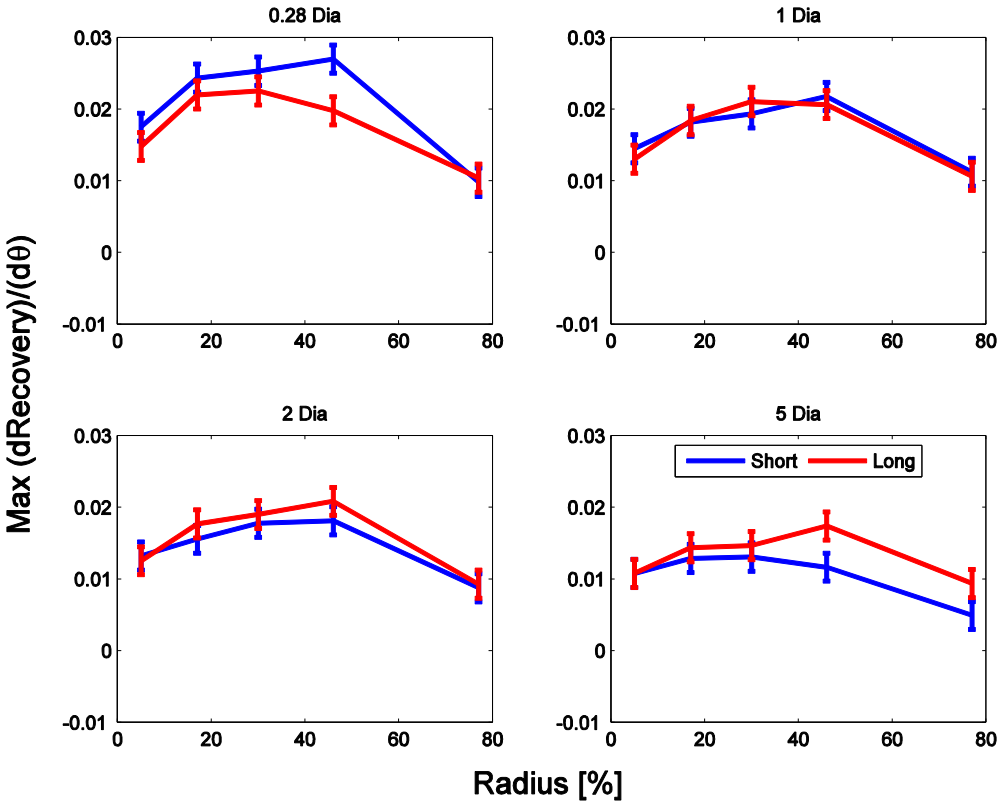

Figure 42. Maximum circumferential gradients for distorted equivalent development lengths and increasing radii.

Higher variations appear in the radial gradients for each circumferential measurement location, as shown in Figure 43. Plot structure is similar to Figure 42 with regards to the subplot placement. The ordinate is given as the recovery gradient for neighboring radii and the abscissa is given as the circumferential location. High radial discrepancies exist for 0.28 duct diameters of development for the 60° and 300° circumferential locations, where there is a large radial transition from a high recovery region for radii < 10% to a low recovery region for radii > 77%. As the profile is given more time to develop (1 to 5 duct diameters), the presence of the fan accelerates the mixing process, resulting in lower overall radial gradients. The upper hemisphere of the distortion profile in the high recovery region ($300^o < \theta < 60^o$) contain higher gradients and the lower hemisphere in the low recovery region ($120^o < \theta < 240^o$) contain lower gradients for the 'long tunnel' configurations, due once again to the increasing mixing rate for screens in closer proximity to the fan face. An increased mixing rate would redistribute the high recovery region into the low recovery pocket, leaving a smaller gradient region from where the flow has left, and creating a higher radial gradient in the region it is migrating to. The 'Short' tunnel configuration shows a rapid decline in radial gradient magnitude from the 1 to 2 duct diameter development lengths, while this sharp reduction is delayed until 5 duct diameters for the 'Long' tunnel configuration.

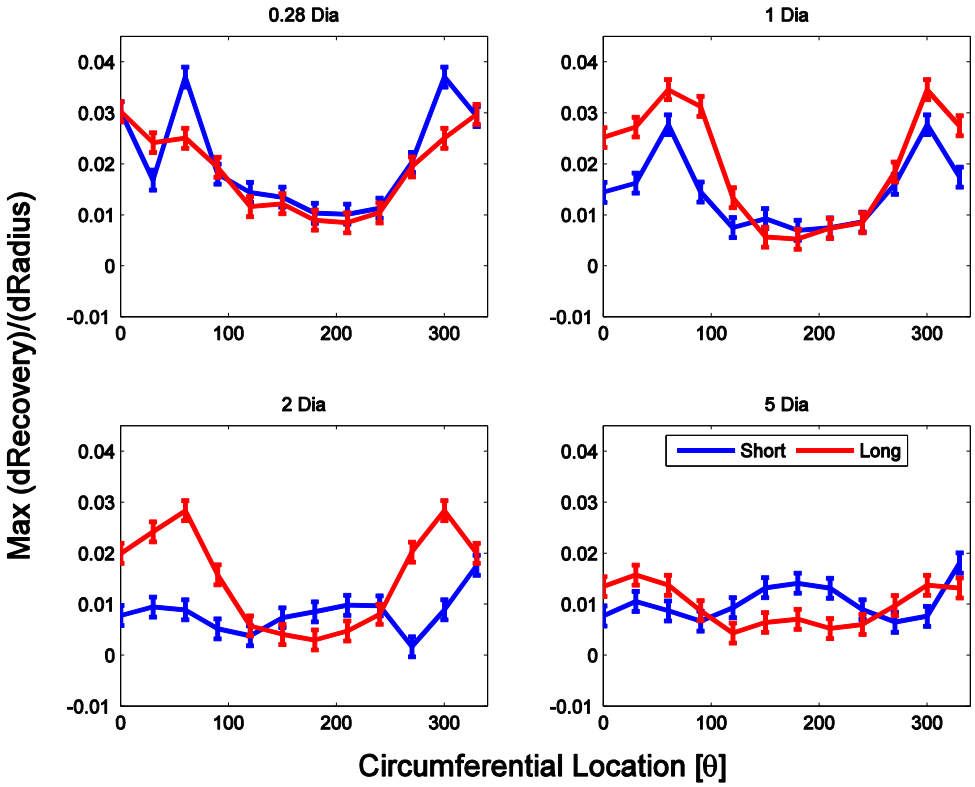

Figure 43. Scatter plot of maximum radial gradients for equivalent development lengths and given circumferential location.

Chapter 6 - Conclusions and Recommendations

A series of experiments were completed on a constant diameter, variable length tunnel to (1) investigate the evolution of a screen-produced total pressure distortion profile and (2) determine the effect of downstream fan presence on this development. Through the use of an engine-powered wind tunnel, a full experimental analysis was completed to understand screen-generated total pressure distortion profile development and screen-fan interaction. Applying this knowledge to upstream distortion profile development will help provide guidance in the design and placement of total pressure distortion screens for ground test applications and distortion-tolerant fan design.

Summary of Results

Part I of this study considered the evolution of a distortion profile in a constant diameter tunnel and how this changes the profile characteristics captured at the measurement plane. Mixing between shear layers of high and low recovery regions is analogous to high momentum entrainment in boundary layer development; the initial low recovery region is 'gaining' energy at the expense of initial high recovery region. Decrease in recovery for radii $\leq$ 25% from the inner wall and recovery increase for radii > 25% for increasing development length. This recovery loss/gain transition occurs closer to the wall for circumferential locations near the initial low recovery deficit region. Proper boundary layer development in the low recovery deficit region is hindered by mixing between high and low recovery regions. Circumferential distortion intensity decreases for increasing development length, at the cost of a wider extent, which converges to a radially uniform value. Radial distortion intensity converges for radii outside of the boundary layer. High circumferential gradients in the transitional regions of the profile create a ripe environment for turbulent mixing, which is highest for radii between 30 and 46%. These gradients decrease for increasing development length across all radii. Due to the evolving nature of the profile, it is recommended to set a measurement plane less than or equal to 1 diameter downstream of the screen plane.

Further development lengths lead to distortion attenuation and merging recovery regions, changing the characteristics of the profile. Also avoided with the short development lengths is the development of a significant boundary layer that reduces the effective cross-sectional area of the duct.

Part II of this study considered the effect of the downstream fan presence on the evolution of the incoming distortion profile. The presence of the fan in close proximity to the screen had no measurable effect on boundary layer development. Higher recovery values were observed for radii $\geq$ 77% for the low recovery and transitional regions for screen placement closer to the fan, which inhibited the mixing between high and low recovery regions for development lengths less than or equal to 1 diameter. For fan/screen placements within 1 duct diameter, the fan acts as a downstream blockage and prevents proper distortion development due to a rising static pressure gradient development developed upstream of the fan and reaching a maximum at the fan face. Circumferential distortion intensity is higher for the short tunnel configurations for radii $\leq$ 46%. Higher radial intensities were observed for radii $\geq$ 77% in the short tunnel configuration. More effective mixing with short tunnel configurations for development lengths greater than 1 duct diameter result in lower circumferential intensity across all radii and a faster convergence of the circumferential extent. Radial distortion intensity remains higher for short configurations at radii $\leq$ 10%, but is consistently lower for radii $\geq$ 77% for development lengths larger than 1 duct diameter. As a result of the fan blockage and effects on the flow, higher circumferential and radial gradients are present for the 0.28 diameter development length. More effective mixing for development lengths greater than 1 duct

diameter reduces these gradients faster for the shorter tunnel configurations. If it is desired for the fan to see the unchanged distortion profile, it is recommended to locate the screen to within 1 duct diameter of the fan face to prevent excessive profile development and ensure the distortion characteristics are not rapidly changing between the measurement plane and the fan face. However, for this case, it is noted that no information was captured for the flow behavior between the TPRA and the fan face.

Future Research Opportunities

Due to spacing limitations impose by the TPRA and the fan face, flow development information between the measurement plane and the fan face was not obtained. As the distortion approaches the fan, the swirling motion of the rotor will add rotational momentum to the profile, adding a co-rotating motion to the distortion. Also, the presence of the spinner cone in front of the rotor, effectively creating a nozzle for the incoming flow, will accelerate and redistribute it into a lower cross-sectional area. The rotation of the engine will likely add a circumferential component to the incoming velocity vector, and the redistribution of the flowfield around the spinner cone will contribute a radial component. Thus, although the total pressure distortion creates a changing incoming axial flow velocity, the addition of the circumferential and radial components creates a true 3-dimensinoal incoming velocity field that must be studied and analyzed. Future research into simulated total pressure distortion patterns should include these components to gain a detailed and accurate understanding of the flow field entering the fan.

Bibliography

[1] Liebeck, R., "Design of the Blended-Wing-Body Subsonic Transport," 40th AIAA Aerospace Sciences Meeting & Exhibit, No. AIAA-2002-0002, AIAA, Reno, Nevada, January 2002.

[2] Plas, A. P., Sargeant, M. A., Madani, V., Crichton, D., Greitzer, E. M., Hynes, T. P., and Hall, C. A., "Performance of a Boundary Layer Ingesting (BLI) Propulsion System," 45th AIAA Aerospace Sciences Meeting & Exhibit , No. AIAA-2007-450, AIAA, Reno, Nevada, January 2007.

[3] Owens, L. R., Allan, B. G., and Gorton, S. A., "Boundary-Layer-Ingesting Inlet Flow Control," 44th AIAA Aerospace Sciences Meeting & Exhibit , No. AIAA-2006-839, AIAA, Reno, Nevada, January 2006.

[4] Daggett, D. L., Kawai, R., and Friedman, D., "Blended Wing Body Systems Studies: Boundary Layer Ingestion Inlets with Active Flow Control," NASA Contractor Report, No. NASA/CR-2003-212670, December 2003, The Boeing Commercial Airplane Group, Seattle, Washington.

[5] Overall, B., "A Procedure for the Design of Complex Distortion Screen Patterns for Producing Specified Steady-State Total Pressure Profiles at the Inlet of Turbine Engines," Tech. rep., Arnold Engineering Development Center, 1972.

[6] Beale, D. K., Cramer, K. B., and King, P. S. "Development of Improved Methods for Simulating Aircraft Inlet Distortion in Turbine Engine Ground Tests," 22nd AIAA Aerodynamic Measurement Technology and Ground Testing Conference, No. AIAA-2002-3045, AIAA, St. Louis, MO, June 2002.

[7] Ferrar, A. Schneck, W., Bailey, J.M., Hoopes, K., O'Brien, W. F., "Application of Additive Manufacturing to Rapidly Produce High-Resolution Total Pressure Distortion Screens," 50th ASM, Nashville, Tennessee, January 9-12, AIAA 2012-0929

[8] Schneck, W. Ferrar, A., Bailey, J.M., Hoopes, K., O'Brien, W. F., "Improved Prediction Method for the Design of High-Resolution Total Pressure Distortion Screens," 51st AIAA ASM, Dallas, Texas, January 7-10, AIAA 2013-1133.

[9] Ferrar, A. and O'Brien, W., "Fan response to total pressure distortions produced by boundary layer ingesting serpentine inlets," 48th AIAA/ASME/SAE/ASEE JPC, Atlanta, Georgia, July 30-August 1 2012, AIAA 2012-3996.

[10] Walter, W.A. and Shaw, M., "Predicted F100 engine response to circumferential pressure and temperature distortion," AIAA Joint Propulsion Conference, June 18-20, Las Vegas, Nevada, 1979

[11] Stenning, A.H. "Inlet distortion effects in axial compressors," Journal of Fluids Engineering, Vol. 102, pp 7-13, March 1980

[12] Govardhan, M. and Viswanath, K. , "Investigations on an axial flow fan stage subjected to circumferential inlet flow distortion and swirl,", Journal of Thermal Science, Vol. 6, No. 4, May 1997

[13] Flitcroft, J.E., Dunham, J., Abbot, W.A. "Transmission of Inlet Distortion through a fan," DTIC Form, No. 463, March 1985.

[14] Henderson, R. E., and Horlock, J. H., 1972, "An Approximate Analysis of the Unsteady Lift on Airfoils in Cascade," ASME J. Eng. Power, 1, pp. 233–240.

[15] Greitzer, E. M., 1973, "Upstream Attenuation and Quasi-Steady Rotor Lift Fluctuations in Asymmetric Flows in Axial Flow Compressors," ASME Paper 73-GT-30.

[16] Fidalgo, V.J., Hall, C.A., and Colin, Y. "A study of fan-distortion interaction within the NASA rotor 67 transonic stage", Journal of Turbomachinery, Vol. 134, September 2012.

[17] Plourde, G. A. and Stenning, A. H., "The Attenuation of Circumferential Inlet Distortion in Multi-Stage Axial Compressors," Journal of Aircraft, Vol. 5, No. 3, May-June, 1968.
[18] Pearson, H. and McKenzie, A. B., "Wakes in Axial Compressors, Journal of the Royal Aeronautical Society, Vol. 63, No. 583,1959, p.415.
[19] G. M. Callahan and A. H. Stenning, "Attenuation of inlet flow distortion upstream of axial flow compressors," in Proceedings of the AIAA 5th Propulsion Joint Specialist Conference, Colo, USA, 1969.
[20] Soeder, R.H. and Bobula, G.A., "Effect of Steady-State Pressure Distortion on Inlet Flow to a High-Bypass-Ratio Turbofan Engine,", NASA Technical Memo, Lewis Research Center, Cleveland, Ohio, October 1982
[21] Berrier, B. L. and Morehouse, M. B., Evaluation of Flush-Mounted, S-Duct Inlets With Large Amounts of Boundary Layer Ingestion," Applied Vehicle Technology Panel Meeting, No. 39, NASA Langley Research Center, NATA Research & Technology Organization, Warsaw, Poland, October 2003.
[22] SAE International. Aerospace recommended practice 1420. January 2001.
[23] Richard Figliola and Donald Beasley. *Theory and Design for Mechanical Measurements.* Wiley, Hoboken, New Jersey, fourth edition, 2006.
[24] [http://www.pwc.ca/files/images/engineFamily/vi_jt15d.png Accessed 2013/03/20]
[25] Callahan, Gary M., "Attenuation of Inlet Flow Distortion Upstream of Axial Flow Compressors," PhD Dissertation, Lehigh University, 1968
[26] Munson, Bruce R., Young, Donald F., and Okiishi, Ted H. *Fundamentals of Fluid Mechanics.* Wiley, Hoboken, New Jersey, fifth edition, 2006.
[27] McArdle, J.G., Jones, W.L., Heidelberg, L.J., and Homyak, L., "Comparison of Several Inflow Control Devices for Flight Simulation of Fan Tone Noise using JT15D-1 Engine," Prepared for the 6th AIAA Aerocoustics Conference, Hartford, Conneticut, June 4-6, 1980.
[28] Falk, Eric A., Jumper, Eric J. Fabian, Michael K., and Stermer, Jerry, 'Upstream-Propagating Potential Disturbances in the F109 Turbofan Engine Inlet Flow', Journal of Propulsion and Power, Vol. 17, No. 2, March – April 2001.
[29] Kozak, Jeffrey D. and Ng, Wing F. 'Investigation of IGV Trailing Edge Blowing in a F109 Turbofan Engine', 38th Aerospace Sciences Meeting & Exhibit, Jan. 10-13, 2000, Reno, NV.
[30] O'Brien, Walter F.,Ng, Wing-fai, and Richardson, Scott M., 'Calculation of Unsteady Fan Rotor Response Caused by Downstream Flow Distortions', Journal of Propulsion and Power, Vol. 1, No. 6, Nov. – Dec., 1985, pp 464 – 469.

Appendix A.1 – Measurement System

The pressure values recorded in this study were recorded using a digital data acquisition system. Sixty Omega PX139 Series pressure transducers with a 5 psi input range and 4 volt output range were employed to measure the incoming total pressure. A National Instruments PXI-6225 multifunction data acquisition (DAQ) card measured the voltage output produced by the transducers and a computer recorded the results.

Table 3 provides the performance specifications of the transducers as provided by the manufacturer and computed pressure uncertainties. All transducers were calibrated at the conclusion of each test according to manufacturer specifications and Virginia Tech Turbomachinery laboratory standards.

Table 3. Measurement uncertainties for pressure transducers.

PX139-005D4V	Uncertainty [% Full Scale (FS)]	Uncertainty [psi]
Linearity and Hysteresis	± 0.1	± 0.005
Repeatability	± 0.3	± 0.015
Zero Temperature Effects	± 0.5	± 0.025
Span Temperature Effects	± 0.5	± 0.025

Appendix A.2 – Uncertainty Calculations

Elemental Systematic Errors

The uncertainty for this experiment occurs due to individual contributions from both the data acquisition system, the digital manometer used to calibrate the transducers, and the transducers themselves. Following the uncertainty calculation methods of Figliola and Beasley [23], the uncertainty in the pressure measurement can be estimated using the rated performance of each component. The first component to consider is the zero-order instrument uncertainty, u_0. This provides an estimate of the expected random uncertainty caused by data scatter when the data acquisition system is recording the voltages outputted from the transducer. Thus, for the PXI-6225 data acquisition card, the uncertainty in the voltage measurements is given in Equation (A-1a).

$$B_{pxi,v} = \pm\frac{1}{2} * resolution \tag{A-1a}$$

$$= \pm 0.5 \times 10^{-6}\ volts \tag{A-1b}$$

The pressure transducers used to record the pressure (Omega PX139) produced a voltage output proportional to the applied pressure over a 4-volt range, from 0.25-4.25V. Equation (A-2) computes the resulting pressure uncertainty for the DAQ card.

$$B_{pxi,psi} = \frac{5\ psi}{4\ volts} * 0.5 \times 10^{-6}\ volts \tag{A-2a}$$

$$= 6.25 \times 10^{-7}\ psi \tag{A-2b}$$

As Equation (A-2b) shows, the uncertainty in the pressure measurement due to the DAQ card is very small. Continuing with the uncertainty calculations as presented in Equation (A-1a) and (A-1b), the resolution uncertainty of the digital manometer used to calibrate the PX139 transducers is computed in Equation (A-3).

$$B_{cal} = \pm 0.0025\ psi \tag{A-3}$$

The instrument uncertainty for the PX139 pressure transducers is computed by combining the elemental errors given in Table (4) using the RMS method [Figliola06]. This is shown in Equations (A-4a-4c).

$$B_{PX139} = \pm\sqrt{\sum_{k=1}^{n} e_k^2} \tag{A-4a}$$

$$B_{PX139} = \pm\sqrt{\left(\frac{0.1 * 5\ psi}{100}\right)^2 + \left(\frac{0.3 * 5\ psi}{100}\right)^2 + \left(\frac{0.5 * 5\ psi}{100}\right)^2 + \left(\frac{0.5 * 5\ psi}{100}\right)^2} \tag{A-4b}$$

$$B_{PX139} = \pm 0.0387\ psi \tag{A-4c}$$

The overall maximum uncertainty is estimated by combining the component uncertainties using the RMS method, shown in Equation (A-5a).

$$B_{total} = \pm\sqrt{u_{PXI,psi}^2 + u_{cal}^2 + u_{PX139}^2} \quad \text{(A-5a)}$$

$$B_{total} = \pm\sqrt{(6.25 \times 10^{-7}\ psi)^2 + (0.0025\ psi)^2 + (0.0387\ psi)^2} \quad \text{(A-5b)}$$

$$B_{total} = \pm 0.0388\ psi \quad \text{(A-5c)}$$

Random Uncertainty

The random uncertainty due to K random measurements can be given by the standard random uncertainty, P. P is estimated by the RSS method and is given below in Equation (A-6)

$$P_i = \sqrt{(P_1^2 + P_2^2 + \cdots + P_k^2)} \quad \text{(A-6)}$$

P can be calculated using a standard random uncertainty about the mean, and represents a measure of the elemental errors affecting the variations in the overall measurement of the dependent variable,

$$P_i = \bar{\sigma}_i = \frac{\sigma}{\sqrt{N}} \quad \text{(A-7)}$$

where N is the number of samples in the data set.

Total Uncertainty

The total uncertainty for each measurement can be determined by combining the systematic elemental uncertainty and the standard random uncertainty. This is given in Equation (A-8).

$$u_{total,i} = \pm\sqrt{(B_{total,i}^2 + \left(t_{v,95}P_{total,i}\right)^2)} \quad (95\%) \quad \text{(A-8)}$$

Error Propagation – Sequential Perturbation

For the calculation of the distortion gradients and the ARP1420 distortion indices; distortion intensity, circumferential extent, and radial intensity, the numerical sequential perturbation method was used to determine the uncertainty. This method is summarized below and follows from Figliola and Beasley [23].

Under a fixed operating condition, calculate a result for all independent variables, R_0, where $R_0 = f(x_1, x_2, \ldots, x_L)$ based on all dependent variables. Establish this as the fixed operating point for the numerical approximation. Next, increase each independent variable by their respective uncertainties and recalculate the result based on each of these new values.

$$R_1^+ = f\left(x_1 + u_{x_1}, x_2, \ldots, x_L\right), \quad \text{(A-9a)}$$

$$R_2^+ = f\left(x_1, x_2 + u_{x_2}, \dots, x_L\right), \dots, \tag{A-9b}$$

$$R_L^+ = f\left(x_1, x_2, \dots, x_L + u_{x_L}\right) \tag{A-9c}$$

Next, repeat the previous calculations but decrease the independent variables by their respective uncertainties and recalculate the result.

$$R_1^- = f\left(x_1 + u_{x_1}, x_2, \dots, x_L\right), \tag{A-10a}$$

$$R_2^- = f\left(x_1, x_2 + u_{x_2}, \dots, x_L\right), \dots, \tag{A-10b}$$

$$R_L^- = f\left(x_1, x_2, \dots, x_L + u_{x_L}\right) \tag{A-10c}$$

Calculate the differences δR_i^+ and δR_i^- for i=1,2,…,L

$$\delta R_i^+ = R_i^+ - R_0 \tag{A-11a}$$

$$\delta R_i^- = R_i^- - R_0 \tag{A-11b}$$

Approximate the uncertainty contribution from each variable,

$$\delta R_i = \frac{\delta R_i^+ - \delta R_i^-}{2} \approx \theta_i u_i \tag{A-12}$$

The final uncertainty can be calculated as.

$$u_R = \pm \sqrt{\left[\sum_{i=1}^{L} (\delta R_i)^2\right]} \tag{A-13}$$